BLACK HOLE SOLUTIONS IN EXTENDED METRIC-PALATINI GRAVITY

by
ELHAM GHORANI

Submitted to the Graduate School of Engineering and Natural Sciences
in partial fulfilment of
the requirements for the degree of Doctor of Philosophy

Sabancı University
July 2025

ABSTRACT

BLACK HOLE SOLUTIONS IN EXTENDED METRIC-PALATINI GRAVITY

ELHAM GHORANI

Physics, Ph.D Dissertation, July 2025

Dissertation Supervisor: Prof. Mehmet Zafer Gedik
Dissertation Co-Supervisor: Dr. Beyhan Puliçe

Keywords: general relativity, Palatini gravity ,geometric Proca, black hole solutions

Extended metric-Palatini gravity, quadratic in the antisymmetric part of the affine curvature, is known to lead to the general relativity plus a geometric Proca field. The geometric Proca, equivalent of the non-metricity vector in the torsion-free affine connection, qualifies to be a distinctive signature of the affine curvature. In this thesis, we explore how photon and particle motion near black holes can be used to probe the geometric Proca field. To this end, we derive static spherically symmetric field equations of this Einstein-geometric Proca theory, and show that it admits black hole solutions in asymptotically AdS background. We perform a detailed study of the optical properties and shadow of this black hole and contrast them with the observational data by considering black hole environments with and without plasma. As a useful astrophysical application, we discuss constraints on the Proca field parameters using the observed angular size of the shadow of supermassive black holes M87* and Sgr A* in both vacuum and plasma cases. We then perform a detailed analysis using the observational quasiperiodic oscillations (QPOs) data. We use the latest data from stellar-mass black hole GRO J1655-40, intermediate-mass black hole in M82-X1, and the super-massive black hole in SgA* (our Milky Way) and perform a Monte-Carlo-Markov-Chain (MCMC) analysis to determine or bound the model parameters. Our results shed light on the allowed ranges of the Proca mass and other parameters. The results imply that our solutions can cover all three astrophysical black holes. Overall, we find that the geometric Proca can be probed via the black hole observations. Our analysis can also be extended to more general metric-affine gravity theories.

ÖZET

GENİŞLETİLMİŞ METRİK-PALATİNİ KÜTLEÇEKİMİNDE KARA DELİK ÇÖZÜMLERİ

ELHAM GHORANI

Fizik, Doktora Tezi, Temmuz 2025

Tez Danışmanı: Prof. Dr. Mehmet Zafer Gedik
Tez Eş Danışmanı: Dr. Beyhan Puliçe

Anahtar Kelimeler: genel görelilik, Palatini kütleçekimi, geometrik Proca, kara delik çözümleri

Antisimetrik eğrilik tensörünün kuadratik terimini içeren genişletilmiş metrik-Palatini kütleçekim teorisi, genel göreliliğe ek olarak geometrik bir Proca alanına yol açtığı bilinmektedir. Bu geometrik Proca alanı, burulmasız afin bağlantıdaki metrik dışı vektörün karşılığı olup, afin eğriliğin ayırt edici bir izi olarak kabul edilebilir. Bu tezde, karadelikler yakınındaki foton ve parçacık hareketlerinin, geometrik Proca alanını nasıl sınayabileceğini araştırıyoruz. Bu amaçla, Einstein-geometrik Proca teorisinin statik ve küresel simetrik alan denklemlerini türetiyor ve bu teorinin asimptotik olarak AdS (anti-de Sitter) arka planında kara delik çözümleri sunduğunu gösteriyoruz. Daha sonra, bu karadeliğin optik özelliklerini ve gölgesini detaylı bir şekilde inceliyor; bu özellikleri, karadelik çevresinde plazma olup olmaması durumlarını dikkate alarak gözlemsel verilerle karşılaştırıyoruz. Astrofiziksel açıdan anlamlı bir uygulama olarak, M87* ve Sgr A* gibi süperkütleli karadeliklerin gözlenen gölge açısını kullanarak Proca alanı parametreleri üzerine kısıtlamalar elde ediyoruz. Ardından, kuasiperiyodik salınım (QPO) verilerini kullanarak kapsamlı bir analiz gerçekleştiriyoruz. Bu kapsamda, yıldız kütleli kara delik GRO J1655-40, orta kütleli kara delik M82-X1, ve Samanyolu'muzdaki süperkütleli karadelik Sgr A* için en güncel verileri kullanıyor ve model parametrelerini belirlemek veya sınırlamak amacıyla Monte Carlo Markov Zinciri (MCMC) analizi uyguluyoruz. Elde ettiğimiz sonuçlar, Proca kütlesi ve diğer parametrelerin izin verilen aralıkları hakkında bilgi sunmaktadır. Sonuçlar, elde ettiğimiz çözümlerin bu üç farklı astrofiziksel kara

deliği açıklayabildiğini göstermektedir. Genel olarak, geometrik Proca alanının kara delik gözlemleri aracılığıyla sınanabilir olduğunu buluyoruz. Bu analiz, daha genel metrik-afin kütleçekim teorilerine de genişletilebilir

ACKNOWLEDGEMENTS

I would first like to express my deepest respect and gratitude to my late supervisor, Prof. Dr. Durmuş Ali Demir, for the trust he placed in me. He constantly guided me with wisdom, and his passion for science was a true source of inspiration. It has been an honor and a privilege not only to know him but also to be his student.

Dr. Beyhan Puliçe was the person with whom I worked most closely during my Ph.D., and I greatly benefited from her experience and guidance. I would like to sincerely thank her for always being accessible, responsive, and humble. Her support made my Ph.D. journey much smoother and easier.

I would like to thank Prof. Dr. Mehmet Zafer Gedik, who kindly accepted to be my supervisor after the loss of my first advisor during my Ph.D. His support and guidance enabled me to continue my doctoral studies without interruption.

I also greatly benefited from the weekly discussions with Prof. Ahmadjon Abdujabbarov, Prof. Farruh Atamurotov, and Prof. Javlon Rayimbaev. Collaborating with them provided me with valuable experience and significantly enriched my research.

I would like to thank the jury members Prof. Kazım Yavuz Ekşi, Prof. Ersin Göğüş, Prof. Tonguç Rador, and Assoc. Prof. Göktuğ Karpat for joining my thesis defense. Their fruitful discussions and constructive feedback contributed directly to this revised version of my thesis.

I would like to thank Mr. Gholam Reza Ebne Ghasem for being a valuable teacher and guide to me from the beginning of my physics journey as an undergraduate until now. I will always consider myself his student.

Finally, I would like to sincerely thank my parents for their unwavering support throughout my life, and my husband, Dr. Bilal Cantürk, for generously sharing his experiences with me. I greatly benefited from his knowledge while writing this thesis.

I gratefully acknowledge the support and full scholarship from Sabancı University.

To my lovely parents,
for their unwavering, warm support and for believing in me.

TABLE OF CONTENTS

LIST OF TABLES

LIST OF FIGURES

1. INTRODUCTION

The question of if the general relativity (GR) is the sole theory of the gravitation is at the heart of the ongoing research in cosmology and astrophysics. In this regard, studying testable extensions of the GR proves particularly useful. One class of extensions concerns higher-order curvature invariants as in, for example, the $f(R)$ gravity (Sotiriou & Faraoni, 2010). One other class involves extension of the metrical geometry of the GR to non-Riemannian geometries based on metric-incompatible connections (Hehl, McCrea, Mielke & Ne'eman, 1995; Schrödinger, 1985; Vitagliano, Sotiriou & Liberati, 2011). Our framework is a special case of such extensions.

The simplest non-Riemannian extension is the *Palatini formulation* (Palatini, 1919), which is characterized by metric $g_{\mu\nu}$ and the Ricci curvature $\mathbb{R}_{\mu\nu}(\Gamma)$ of a general symmetric affine connection $\Gamma^{\lambda}_{\mu\nu}$ (a torsion-free connection independent of the metric $g_{\mu\nu}$ and its Levi-Civita connection ${}^{g}\Gamma^{\lambda}_{\mu\nu}$). This formulation gives the Einstein field equations with no need to extrinsic curvature (Gibbons & Hawking, 1977a; York, 1972). With general curvature invariants, it leads to the GR along with geometrical scalars, vectors and tensors (Karahan, Dogangun & Demir, 2012). The relevance of the Palatini gravity for emergent gravity theories (Demir, 2019,2) is it's another application area. It was shown that the extension of the Palatini gravity with fundamental scalars like the Higgs field leads to natural inflation (Bauer & Demir, 2008,1). Higher-curvature terms were also studied in the Palatini formalism (Demir & Puliçe, 2020; Vitagliano, 2014; Vitagliano et al., 2011) and their certain effects in astrophysics and cosmology were analysed in (Sotiriou & Liberati, 2007).

One step further from the Palatini formulation is the inclusion of a term like $\mathbb{R}_{[\mu\nu]}(\Gamma)\mathbb{R}^{[\mu\nu]}(\Gamma)$, where $\mathbb{R}_{[\mu\nu]}(\Gamma)$ is the anti-symmetric part of the affine Ricci tensor $\mathbb{R}_{\mu\nu}(\Gamma)$. What is important about this inclusion is that it leads dynamically to the GR plus a purely geometric massive vector field Q_{μ} (Demir & Puliçe, 2020; Vitagliano, Sotiriou & Liberati, 2010). This vector field, a *geometric Proca field* as we will call it henceforth, is defined as $Q_{\mu} \equiv \frac{1}{4} Q_{\mu\nu}{}^{\nu}$ where $Q_{\lambda\mu\nu} \equiv -{}^{\Gamma}\nabla_{\lambda} g_{\mu\nu}$ is the non-metricity tensor (Buchdahl, 1979; Demir & Puliçe, 2020; Obukhov, Vlachynsky, Esser & Hehl, 1997; Tucker & Wang, 1996; Vitagliano et al., 2010). (We call

non-metricity vector as geometric Proca to distinguish it from the generic Einstein-Proca system as well as the generic Z' bosons in the literature.) With a symmetric affine connection (torsion-free), one is left with a special case of non-Riemannian geometries in which non-metricity $Q_{\lambda\mu\nu}$ is the only source of the deviations from the GR. This special case is the Weyl gravity (Romero, Fonseca-Neto & Pucheu, 2012; Scholz, 2017; Vitagliano, 2014; Weyl, 1918) (see also gauge invariance analysis in (O'raifeartaigh & Straumann, 2000)). The geometric Proca is a direct signature of the Weyl gravity. More specifically, it is signature of metric-incompatible symmetric connections (torsion-free). It is not something put by hand. It is not something that comes from gauge theories either. It is a geometrical massive vector field that characterizes the Weyl nature of the geometry (Romero et al., 2012; Scholz, 2017). It has been studied as vector dark matter in (Demir & Puliçe, 2020). Its couplings to fermions (quarks and leptons) were explored in (Demir & Puliçe, 2022) in regard to the black hole horizon in the presence of the Proca field (Obukhov et al., 1997).

One step further from the Palatini formalism with the geometric Proca Q_μ is the inclusion of the metrical curvature $R_{\mu\nu}({}^g\Gamma)$ in addition to the already-present affine curvature $\mathbb{R}_{\mu\nu}(\Gamma)$. Excepting the quadratic term $\mathbb{R}_{[\mu\nu]}(\Gamma)\mathbb{R}^{[\mu\nu]}(\Gamma)$ leading to the geometric Proca field, this combined metric-affine framework is the *metric-Palatini* gravity (Capozziello, Harko, Koivisto, Lobo & Olmo, 2013b,1; Harko, Koivisto, Lobo & Olmo, 2012). This formalism, a direct combination of the metrical and Weyl gravities, helps relaxing the constraints on the Proca mass (as discussed in (Demir & Puliçe, 2022) in comparison to (Demir & Puliçe, 2020)). The metric-Palatini gravity, excepting $\mathbb{R}_{[\mu\nu]}(\Gamma)\mathbb{R}^{[\mu\nu]}(\Gamma)$ term considered in the present work, has already been studied in regard to dark matter (Capozziello, Harko, Koivisto, Lobo & Olmo, 2013c), wormholes (Capozziello, Harko, Koivisto, Lobo & Olmo, 2012), and cosmology (Capozziello, Harko, Koivisto, Lobo & Olmo, 2013a).

The gravity theory we explore in this thesis is the metric-Palatini gravity extended with the $\mathbb{R}_{[\mu\nu]}(\Gamma)\mathbb{R}^{[\mu\nu]}(\Gamma)$ invariant and a negative cosmological constant (CC). Indeed, as it was made clear in (Demir & Puliçe, 2022), in the presence of the geometric Proca Q_μ, the CC is a necessity for having black hole solutions. Our framework, which we call *extended metric-Palatini gravity* (EMPG), possesses these four basic properties:

(1.1)
- (i) It is linear in affine curvature scalar $g^{\mu\nu}\mathbb{R}_{\mu\nu}(\Gamma)$,
- (ii) It is torsion-free ($\Gamma^\lambda_{\mu\nu} = \Gamma^\lambda_{\nu\mu}$),
- (iii) It involves the invariant $\mathbb{R}_{[\mu\nu]}(\Gamma)\mathbb{R}^{[\mu\nu]}(\Gamma)$,
- (iv) It contains a negative CC.

Given these properties, the EMPG action takes the schematic form (whose exact form will be discussed in Chapter 2)

$$S[g,\Gamma]=\int d^4x\sqrt{-g}\quad\Big\{\text{“}g^{\mu\nu}R_{\mu\nu}\,(^g\Gamma)\,\text{”}+\text{“}g^{\mu\nu}\mathbb{R}_{\mu\nu}\,(\Gamma)\,\text{”}$$
$$+\text{“}\mathbb{R}_{[\mu\nu]}(\Gamma)\mathbb{R}^{[\mu\nu]}(\Gamma)\text{”}+\text{“CC”}\Big\} \tag{1.2}$$

in which $R_{\mu\nu}\,(^g\Gamma)$ and $\mathbb{R}_{\mu\nu}\,(\Gamma)$ are, respectively, the metrical and affine Ricci curvatures. The EMPG is an Einstein-geometric Proca-Anti de Sitter (AdS) system. We will constrain its parameters and dynamics by using the observational data on black holes. In fact, in the literature, Einstein-Proca system (not the geometric Proca in the present work) has been analyzed for finding Reissner-Nordström type spherically-symmetric vacuum solutions (Macías & Socorro, 1999; Tresguerres, 1995; Tucker & Wang, 1995; Vlachynsky, Tresguerres, Obukhov & Hehl, 1996), for determining the role of the Proca field (Adler & Pearson, 1978; Bekenstein, 1972a,7), for obtaining spherically-symmetric static solutions (Frolov, 1978; Gottlieb, Hojman, Rodríguez & Zamorano, 1984; Leaute & Linet, 1985), and for revealing the structure of the horizon radius (Ayón-Beato, García, Macías & Quevedo, 2000; Obukhov & Vlachynsky, 1999; Toussaint, 2000). In view of this rich literature, construction and analysis of the Einstein-geometric Proca-AdS black holes in the present work can probe affine curvature, with various applications in other astrophysical and cosmological phenomena. In essence, in the present work, we are probing, for the first time in the literature, non-metricity tensor via the Einstein-geometric Proca-AdS black holes.

One of the consequences of the light propagation in curved spacetime is the appearance of the shadow of the black hole (BH). If the BH is located between the light source and the observer, then due to the capturing the part of the light by the central object observer detect the black spot in the bright background on the celestial plane. This black spot is referred to as BH shadow and first theoretically predicted by Synge (Synge, 1960) and further developed by Luminet (Luminet, 1979) and Bardeen (Bardeen, 1973). Even before the first ever observation of the BH shadow in 2019 by the Event Horizon Telescope collaboration (Akiyama & others, 2019a,1) various authors have studied the shadow of the black hole/compact objects within general relativity and modified/alternative theories of gravity (see, e.g. (Bambi & Freese, 2009; Perlick, Tsupko & Bisnovatyi-Kogan, 2018)) and also the authors studied the effect of plasma on the BH shadow in (Atamurotov, Jusufi, Jamil, Abdujabbarov & Azreg-Aïnou, 2021; Perlick, Tsupko & Bisnovatyi-Kogan, 2015). Observation data on the shadow of supermassive BHs at the center of M87(Akiyamaet al.

, 2019a) and Sgr A*(Akiyama & others, 2022) are used to get estimations and/or constraints of BH parameters within different gravity models (Vagnozzi & others, 2023).

In fact, despite large uncertainties of black hole shadow size including the mass and distance measurements, astrophysical observation related to black holes shadows in strong and weak gravity regimes is helpful in testing gravity theories. The first black hole shadow has been observed by Event Horizon Telescope observing at a wavelength of 1.3 mm, in 2019, the image of M87* (which has 6.5±0.7 billion solar masses, located at 16.8 kpc) with the angular size 42±3 μas with the observational resolution 20 μas (Akiyamaet al. , 2019a). Three years later, in 2022, the image of the central part of the Milky Way galaxy, known as Sgr A* (with $4^{+1.1}_{-0.6}$ million solar masses, located at about 8 kpc), has also been observed with shadow size 48.7±7 μas together with the radiation ring with the size 51.8±2.3 μas (Akiyamaet al. , 2022). The appearance of the radiation ring may be due to the presence of a plasma medium around Srg A*. Therefore, studies of the gravitational lensing effects of black holes including plasma is important. We study photon motion around the BH in the EMGP model to determine the optical properties of black holes and the black hole shadow. Then we determine constraints on the EMPG parameters using the observational image size of the supermassive black holes M87* and Sgr A*.

The next step is to extend our work by determining constraints on the EMPG parameters from the QPOs. Analyzing the spectroscopic properties of radiation released by accreting matter in the neighborhood of gravitational compact objects, such as black holes, wormholes, and neutron stars, is one possible way to investigate the properties of the spacetime around them. The radiation processes around the accretion disk are shaped mainly by the gravitational pull of the black hole in binary systems where neutron stars or black holes coexist with their companion stars. The continuous X-ray data from these accretion disks in (micro)quasars can be Fourier-analyzed (Stella & Vietri, 1998; Stella, Vietri & Morsink, 1999a) to reveal the existence of QPOs (quasi-periodic oscillations). The QPOs are categorized as high frequency (HF) when their peak frequencies fall within the range of approximately 0.1 to 1 kilohertz (kHz) and as low frequency (LF) when their frequencies are below about 0.1 kHz (Stuchlík, Slaný & Hledík, 2000).

Accurate measurements of QPO frequencies in quasars and binary systems (microquasars) have shed light on the physical processes driving their formation. This ongoing study attempts to determine the properties of the accretion disk's inner edge and test different theories of gravity in this way. These tests can potentially yield measurements concerning the black hole properties and the radii of nearby

ISCOs. Previous research has demonstrated that investigating the QPO orbit can be instrumental in inferring the radius of the ISCO lying close to the QPO orbit (Rayimbaev, Abdujabbarov & Wen-Biao, 2021; Rayimbaev, Bokhari & Ahmedov, 2022). Notably, the relativistic precision model indicates that the distance between these orbits is within the measurement error range.

We begin Chapter 2 with a brief review of two formulations of GR: the metric and Palatini formulations. We then present an extention of Palatini formalisim (EMPG) and provide a detailed analysis of the EMPG, starting with a ghost-free Lagrangian in the AdS background. We show that the EMPG gravity dynamically reduces to the GR plus a geometric Proca field (the non-metricity vector from the rank-3 non-metricity tensor). We give static, spherically-symmetric solutions of the EMPG and apply our results to determine the Einstein-geometric Proca-AdS black hole solutions.

In chapter 3, we study photon motion around a compact object in the EMPG model to determine the optical properties of black holes and the black hole shadow. We finish the chapter by determining constraints on the EMPG parameters using the observational image size of the supermassive black holes M87* and Sgr A*.

In chapter 4, particle dynamics around Einstein-Geometric Proca-AdS compact object is studied. The fundamental frequencies of circular orbits are presented. Then, we investigate QPOs and determine the constraints on the EMPG parameters using observational data from the twin peak QPOs.

2. EMPG BLACK HOLES

In this chapter, we explore an extension of GR called Extended Metric-Palatini Gravity (EMPG) and its black hole solution. We begin by reviewing the metric and Palatini formulations of General Relativity, emphasizing their conceptual and technical differences. Building on the Palatini approach, we introduce a novel extension (EMPG) which incorporates the antisymmetric part of the affine Ricci tensor. We show that this framework reduces to General Relativity plus a massive vector field (geometric Proca), effectively forming an Einstein–Geometric Proca system. We analyze the structure and dynamics of this theory, derive its field equations, and obtain static, spherically symmetric black hole solution in an AdS background. The physical and geometric properties of these solutions are then studied in detail.

2.1 Metric and Palatini Formulations of General Relativity

Einstein originally formulated General Relativity as a theory in which the dynamics of spacetime are governed by the metric tensor $g_{\mu\nu}$ and its associated Levi-Civita connection, defined by

$$ {}^{g}\Gamma^{\lambda}_{\mu\nu} = \frac{1}{2} g^{\lambda\rho} \left(\partial_\mu g_{\nu\rho} + \partial_\nu g_{\rho\mu} - \partial_\rho g_{\mu\nu} \right). \tag{2.1} $$

The Einstein Field Equations can be derived from the Einstein-Hilbert action via the principle of stationary action. The gravitational part of the action is

$$ S[g] = \int d^4x \sqrt{-g} \frac{M_{Pl}^2}{2} R({}^{g}\Gamma), \tag{2.2} $$

where $g = det(g_{\mu\nu})$, M_{Pl} is the Plank mass and $R(g) \equiv g^{\mu\nu} R_{\mu\nu}({}^{g}\Gamma)$ is the Ricci scalar. The Ricci scalar is obtained by contracting the Ricci tensor, which in turn

is constructed from the Levi-Civita connection

$$R_{\mu\nu}({}^{g}\Gamma) = \partial_\lambda \Gamma^\lambda_{\mu\nu} - \partial_\nu \Gamma^\lambda_{\lambda\mu} + \Gamma^\rho_{\rho\lambda}\Gamma^\lambda_{\mu\nu} - \Gamma^\rho_{\nu\lambda}\Gamma^\lambda_{\rho\mu} \tag{2.3}$$

The Einstein-Hilbert action alone does not yield the Einstein field equations from the variational principle unless a boundary term is added (Gibbons & Hawking, 1977a; York, 1972). This boundary term, which involves the extrinsic curvature of the boundary, ensures that the action is well-defined when the metric is fixed at the boundary. A well-known solution to this problem is the Palatini formalism (Palatini, 1919), in which the Levi-Civita connection ${}^{g}\Gamma^\lambda_{\mu\nu}$ is replaced by a more general, symmetric affine connection $\Gamma^\lambda_{\mu\nu}$. In this approach, the metric and the connection are treated as independent variables during the variation of the action. The Ricci tensor $R({}^{g}\Gamma)$ in (2.2) is substituted by $\mathbb{R}(g,\Gamma)$ which is a function of both metric $g_{\mu\nu}$ and affine connection $\Gamma^\lambda_{\mu\nu}$. Then the Einstein-Hilbert action takes the form

$$S[g,\Gamma] = \int d^4x\sqrt{-g}\frac{M_{Pl}^2}{2}\mathbb{R}(g,\Gamma)\,. \tag{2.4}$$

Variation of $S[g,\Gamma]$ with respect to metric $g_{\mu\nu}$ yields the Einstein field equations in vacuum,

$$R_{\mu\nu} - \frac{1}{2}Rg_{\mu\nu} = 0, \tag{2.5}$$

while the variation with respects to the affine connection $\Gamma^\lambda_{\mu\nu}$ gives rise to the **metricity condition**

$$\nabla_\lambda g_{\mu\nu} = 0. \tag{2.6}$$

which, in the metric formulation of General Relativity, was assumed a priori. The solution to (2.6) is the Levi-Civita connection, implying that the Palatini formalism recovers the standard Einstein field equations and thus provides a consistent variational framework for General Relativity.

2.2 From Palatini Formulation to Einstein-Geometric Proca System

In this subsection, we first extend the Palatini action (2.4) by including the antisymmetric part of the affine Ricci tensor. We then demonstrate that this extension—referred to as **Extended Metric-Palatini Gravity (EMPG)**—leads to General Relativity supplemented by a massive, purely geometric vector field (geometric Proca). This framework, known as the **Einstein–Geometric Proca** model, effectively describes a geometric realization of a Proca field emerging from the underlying spacetime geometry.

The EMPG model, defined schematically in (1.2), takes its exact form (Demir & Puliçe, 2020; Demir & Puliçe, 2022)

$$\begin{aligned} S[g,\Gamma] \quad &= \int d^4x\sqrt{-g}\Bigg\{ \frac{M^2}{2}R(g) + \frac{\overline{M}^2}{2}\mathbb{R}(g,\Gamma) + \xi\overline{\mathbb{R}}_{\mu\nu}(\Gamma)\overline{\mathbb{R}}^{\mu\nu}(\Gamma) \\ &\quad -V_0 + \mathcal{L}_m({}^g\Gamma,\psi)\Bigg\}, \end{aligned} \tag{2.7}$$

with an action based on the metric tensor $g_{\mu\nu}$ like the GR and on a symmetric affine connection $\Gamma^\lambda_{\mu\nu} = \Gamma^\lambda_{\nu\mu}$ unlike the GR. The affine connection is independent of the Levi-Civita connection (2.1) generated by the metric $g_{\mu\nu}$. The Levi-Civita connection sets the covariant derivative ∇_μ such that $\nabla_\alpha g_{\mu\nu} = 0$. It also sets the Ricci curvature $R_{\mu\nu}({}^g\Gamma)$, which contracts to give the scalar curvature $R(g) \equiv g^{\mu\nu}R_{\mu\nu}({}^g\Gamma)$. The affine connection $\Gamma^\lambda_{\mu\nu}$, on the other hand, is independent of the metrical connection ${}^g\Gamma^\lambda_{\mu\nu}$, defines the covariant derivative ${}^\Gamma\nabla_\mu$, and sets the Riemann curvature

$$\mathbb{R}^\mu_{\alpha\nu\beta}(\Gamma) = \partial_\nu\Gamma^\mu_{\beta\alpha} - \partial_\beta\Gamma^\mu_{\nu\alpha} + \Gamma^\mu_{\nu\lambda}\Gamma^\lambda_{\beta\alpha} - \Gamma^\mu_{\beta\lambda}\Gamma^\lambda_{\nu\alpha}, \tag{2.8}$$

with $\mathbb{R}^\mu_{\alpha\nu\beta}(\Gamma) = -\mathbb{R}^\mu_{\alpha\beta\nu}(\Gamma)$. Its contractions lead to two distinct Ricci curvatures $\mathbb{R}_{\mu\nu}(\Gamma) = \mathbb{R}^\lambda_{\mu\lambda\nu}(\Gamma)$ and $\overline{\mathbb{R}}(\Gamma) = \mathbb{R}^\lambda_{\lambda\mu\nu}(\Gamma)$. The latter is actually the antisymmetric part of the former

$$\overline{\mathbb{R}}_{\mu\nu}(\Gamma) = \mathbb{R}_{[\mu\nu]}(\Gamma) = \partial_\mu\Gamma^\rho_{\rho\nu} - \partial_\nu\Gamma^\rho_{\rho\mu}, \tag{2.9}$$

and does necessarily vanish when the affine connection $\Gamma^\lambda_{\mu\nu}$ is replaced with the metrical one ${}^g\Gamma^\lambda_{\mu\nu}$. The total affine Ricci curvature leads to the affine scalar curvature $R(g,\Gamma) \equiv g^{\mu\nu}\mathbb{R}_{\mu\nu}(\Gamma)$ (Bauer & Demir, 2008; Karahan et al., 2012).

The action (2.7) is composed of physically distinct parts (Demir & Puliçe, 2022). The

first part proportional to M^2 would be the usual Einstein-Hilbert action if M were equal to the Planck mass M_{Pl}. The second term proportional to $\overline{M}^2$ is the standard Palatini action (Palatini, 1919), which leads to the Einstein field equations with no need for extrinsic curvature (Gibbons & Hawking, 1977a; York, 1972). The third term proportional to ζ was considered in both (Vitagliano et al., 2010) and (Demir & Puliçe, 2020). The fourth term V_0 is the vacuum energy not considered in (Demir & Puliçe, 2022) (It is proportional to the CC in (1.2) in Introduction). The matter Lagrangian $\mathcal{L}_m({}^g\Gamma, \psi)$ governs the dynamics of the matter fields ψ (matter sectors involving $\Gamma^\lambda_{\mu\nu}$ (not ${}^g\Gamma^\lambda_{\mu\nu}$) have been analyzed in (Demir & Puliçe, 2020)). Our setup differs from the so-called metric-Palatini setup (Capozziello et al., 2013b,1; Harko et al., 2012) by the third term proportional to ζ (and dropping of the higher powers of $R_{\mu\nu}({}^g\Gamma)$ and $\mathbb{R}_{\mu\nu}(\Gamma)$ in view of gravitational ghosts). **We call this framework Extended metric-Palatini gravity or in short EMPG.**

In non-Riemannian geometries with symmetric connections ($\Gamma^\lambda_{\mu\nu} = \Gamma^\lambda_{\nu\mu}$) the torsion vanishes identically. Then, the difference between such geometries and the metrical geometry of the GR (Obukhov et al., 1997; Tucker & Wang, 1996; Vitagliano et al., 2010)

$$\Gamma^\lambda_{\mu\nu} - {}^g\Gamma^\lambda_{\mu\nu} = \frac{1}{2} g^{\lambda\rho}(Q_{\mu\nu\rho} + Q_{\nu\mu\rho} - Q_{\rho\mu\nu}), \tag{2.10}$$

is sourced by the **non-metricity tensor**

$$Q_{\lambda\mu\nu} = -{}^\Gamma\nabla_\lambda g_{\mu\nu}, \tag{2.11}$$

as a measure of the metric-incompatibility of the affine connection $\Gamma^\lambda_{\mu\nu}$. In fact, non-metricity is the main feature of the Weyl geometry (O'raifeartaigh & Straumann, 2000; Romero et al., 2012; Scholz, 2017). The use of the affine connection in (2.10) in the action (2.7) and the use also of the equation of motion for the non-metricity tensor in (2.11) leads one to the reduced action (Demir & Puliçe, 2020; Demir & Puliçe, 2022; Vitagliano et al., 2010)

$$\begin{aligned} S[g, Y, \psi] \;=\; & \int d^4x\sqrt{-g}\Bigg\{ \frac{1}{16\pi G_N} R(g) - \frac{1}{4} Y_{\mu\nu}Y^{\mu\nu} - \frac{1}{2} M_Y^2 Y_\mu Y^\mu \\ & - V_0 + \mathcal{L}_m(g, {}^g\Gamma, \psi)\Bigg\}, \end{aligned} \tag{2.12}$$

in which $Q_\mu = Q^\nu_{\mu\nu}/4$ is the non-metricity vector, $Y_\mu = 2\sqrt{\xi}Q_\mu$ is the canonical

geometric vector field, $G_N = 8\pi/(M^2 + \overline{M}^2)$ is Newton's gravitational constant, and

$$M_Y^2 = \frac{3\overline{M}^2}{2\xi} \tag{2.13}$$

is the squared-mass of the Y_μ (the geometric Proca field). We now bring the EMPG action (2.12) into a more compact form

$$S[g,Y] = \int d^4x\sqrt{-g}\frac{1}{2\kappa}\left\{R(g) - 2\Lambda - M_Y^2\hat{Y}_\mu\hat{Y}^\mu - \frac{1}{2}\hat{Y}_{\mu\nu}\hat{Y}^{\mu\nu}\right\}, \tag{2.14}$$

in which $\kappa = 8\pi G_N$, $\Lambda = \kappa V_0$ is the CC in (1.2), and $\hat{Y}_\mu \equiv \sqrt{\kappa}Y_\mu$ is the canonical dimensionless Proca field. We call the system introduced by the action (2.14) **Einstein-geometric Proca model.**

The actions (2.12) and (2.14) are readily recognized to belong to the Weyl geometry with Weyl vector Y_μ (O'raifeartaigh & Straumann, 2000; Romero et al., 2012; Scholz, 2017). It should nevertheless be kept in mind that neither the schematic action (1.2) nor the exact action (2.7) nor the reduced Weyl action (2.12) are conformal-invariant. The reason is that the EMPG, beginning from (1.2), is based on the Ricci curvatures and the CC not the Weyl tensor $W^\lambda_{\mu\nu\rho}$ whose quadratic is conformal-invariant. (Conformal transformations in Weyl gravity have been discussed in (Flanagan, 2006; Karahan et al., 2012).)

Variation of the action (2.14) with respect to the metric $g_{\mu\nu}$ leads to the Einstein field equations

$$R_{\mu\nu} - \Lambda g_{\mu\nu} - \hat{Y}_{\alpha\mu}\hat{Y}^\alpha{}_\nu + \frac{1}{4}\hat{Y}_{\alpha\beta}\hat{Y}^{\alpha\beta}g_{\mu\nu} - M_Y^2\hat{Y}_\mu\hat{Y}_\nu = 0, \tag{2.15}$$

and its variation with respect to $\hat{Y}_\mu$ gives the Proca equation

$$\nabla_\mu\hat{Y}^{\mu\nu} - M_Y^2\hat{Y}^\nu = 0, \tag{2.16}$$

describing $\hat{Y}_\mu$ as a free dimensionless massive vector field. **This thesis aims to investigate the geometric Proca field $\hat{Y}_\mu$, representing the non-metricity of spacetime, by studying the black hole solutions in the model.**

2.3 Black Hole Solutions in the Extended Metric-Palatini Gravity

In this subsection we will solve the field equations (2.15) and (2.16). In an attempt to find spherically-symmetric static solutions of the field equations in space coordinates (r, θ, ϕ), we put forth the ansatz

$$g_{\mu\nu} = \mathrm{diag}(-h(r), \frac{1}{f(r)}, r^2, r^2 \sin^2\theta). \tag{2.17}$$

Having done with the metric, the geometric Proca field Y_μ obeying the equation of motion (2.16) can be taken as a purely time-like field

$$\hat{Y}_\mu = \hat{\phi}(r)\delta^0_\mu, \tag{2.18}$$

in agreement with a spherically-symmetric background. With this time-like vector, the gravitational and geometric-Proca parts of the EMPG model are described by three real functions $h(r), f(r)$ and $\phi(r)$.

In order to have a dimensionless equation's system, we define the following dimensionless quantities:

$$\hat{r} := \kappa^{-1/2} r, \;\; \hat{M}_Y^2 := \kappa M_Y^2 \;. \tag{2.19}$$

So that along with $\hat{Y}_\mu$ the entire system gets expressed in terms of the dimensionless quantities.

Substituting metric ansatz (2.17) and Proca field (2.18) into the field equations (2.15) and (2.16) yields the corresponding differential equations. The subtraction of the $(\mu\nu = 00)$ and $(\mu\nu = 11)$ components of the Einstein equations (2.15) accordingly leads to the following equation

$$\hat{\phi}^2 = \frac{1}{\hat{M}_Y^2 \hat{r}}(fh' - f'h). \tag{2.20}$$

The $(\mu\nu = 22)$ component of the Einstein field equations (2.15) reads as

$$1 - f - \frac{\hat{r}(hf)'}{2h} - \Lambda\hat{r}^2 - \frac{f\hat{r}^2}{2h}\hat{\phi}'^2 = 0. \tag{2.21}$$

The Proca equation of motion (2.16) becomes

$$\frac{\sqrt{hf}}{\hat{r}^2}\left(\hat{r}^2\sqrt{\frac{f}{h}}\hat{\phi}'\right)' - \hat{M}_Y^2\hat{\phi} = 0 \ . \tag{2.22}$$

In order to have an idea of what solution to expect we first solve the Proca equation (2.22) in the flat spacetime limit ($f(\hat{r}) = h(\hat{r}) = 1$). This corresponds to setting the cosmological constant Λ equal to zero. In this particular limit we find that

$$\hat{\phi}^{(flat)}(\hat{r}) = c_1\frac{e^{-\hat{M}_Y\hat{r}}}{\hat{r}} + c_2\frac{e^{\hat{M}_Y\hat{r}}}{\hat{r}} \ , \tag{2.23}$$

which is what is expected of a Yukawa potential (massive vector field) in the flat spacetime. According to (2.23), Proca field is not well-defined as $r \to 0$ and $r \to \infty$ in the flat background.

Now, we turn to curved AdS geometry, which arises from the presence of a negative cosmological constant Λ, in the weak field limit. In this limit, we take the metric functions in the form

$$h(\hat{r}) = f(\hat{r}) = 1 + \frac{\hat{r}^2}{l^2}, \tag{2.24}$$

after letting $\Lambda = -\frac{3}{l^2}$ in (2.14) in which l stands for the AdS radius. In this case, the Proca equation (2.22) takes the form

$$\frac{1}{\hat{r}^2}(1 + \frac{\hat{r}^2}{l^2})(\hat{r}^2\phi')' = \hat{M}_Y^2\hat{\phi}, \tag{2.25}$$

with the exact solution

$$\begin{aligned}\hat{\phi}(\hat{r}) = \frac{l}{\hat{r}}c_1\ {}_2F_1\left(\frac{-1-\sigma}{4}, \frac{-1+\sigma}{4}, \frac{1}{2}, -\frac{\hat{r}^2}{l^2}\right) \\ +c_2\ {}_2F_1\left(\frac{1-\sigma}{4}, \frac{1+\sigma}{4}, \frac{3}{2}, -\frac{\hat{r}^2}{l^2}\right) \ ,\end{aligned} \tag{2.26}$$

where

$$\sigma = \sqrt{1 + 4\hat{M}_Y^2 l^2} \ . \tag{2.27}$$

The Breitenlohner-Freedman window of non-tachyonic negative mass-squared values lies in the following range

$$m_{BF}^2 \leq \hat{M}_Y^2 < 0, \tag{2.28}$$

where

$$m_{BF}^2 = -\frac{1}{4l^2} \tag{2.29}$$

is the Breitenlohner-Freedman mass bound which is required to avoid tachyonic run-away instabilities in the AdS background. The range of parameter σ accordingly is

$$0 \leq \sigma < 1. \tag{2.30}$$

Expanding $\hat{\phi}(\hat{r})$ around infinity the Proca field (2.26) takes the following form

$$\hat{\phi}(\hat{r}) = \frac{q_1}{\hat{r}^{\frac{1-\sigma}{2}}} + \frac{q_2}{\hat{r}^{\frac{1+\sigma}{2}}} \ . \tag{2.31}$$

It is clear that in the Maxwell limit ($\sigma \to 1$) this Proca field behaves as $\hat{\phi}(\hat{r}) \to q_1 + \frac{q_2}{\hat{r}}$ and it means that q_2 has the meaning of an electromagnetic-like charge while q_1 represents a uniform potential.

Due to the back-reaction of the Proca field in (2.31) on the spacetime geometry, the metric potentials are expected to get modified as follows

$$\begin{aligned} f(\hat{r}) &= \hat{r}^2 l^{-2} + 1 + \frac{n_1}{\hat{r}^{1-\sigma}} + \frac{n_2}{\hat{r}} \ , \\ h(\hat{r}) &= \hat{r}^2 l^{-2} + 1 + \frac{m_1}{\hat{r}^{1-\sigma}} + \frac{m_2}{\hat{r}} \ , \end{aligned} \tag{2.32}$$

in which the higher inverse powers of $\hat{r}$ have been ignored. En passant, one notices that the AdS geometry makes the Proca field to have the Coulombic form in (2.31) in place of the Yukawa form in (2.23) of the flat spacetime. The parameters n_1, n_2 and m_1 are found in terms of q_1, q_2 and m_2 by substituting (2.31) and (2.32) into the equations of motion

$$n_1 = \frac{(1-\sigma)}{4} q_1^2, \quad n_2 = m_2 - \frac{(1-\sigma)(1+\sigma)}{6} q_1 q_2, \quad m_1 = \frac{(1-\sigma)}{3-\sigma} q_1^2 \tag{2.33}$$

where q_1, q_2 and m_2 are free parameters. The solution (2.32), together with (2.33), describes **Einstein-Geometric Proca AdS black hole**s. In the limit of $q_1 = 0$ we have

$$n_1 = m_1 = 0, \quad n_2 = m_2. \tag{2.34}$$

This reduces the metric functions (2.32) to

$$f(\hat{r}) = h(\hat{r}) = 1 + \frac{\hat{r}^2}{l^2} + \frac{n_2}{\hat{r}}, \tag{2.35}$$

which describes **AdS-Schwarzschild black holes** when $n_2 = -2M$, with M being the black hole mass. In the next subsection, by calculating the mass of the solution (2.32), we find m_2 in terms of Proca parameters q_1, q_2 as well.

2.3.1 Black Hole Mass

To compute the mass of the solution, we begin by calculating the energy-momentum tensor $T_{\mu\nu}$. Then integration of T_{00} will give us the mass. We employ the method suggested by Balasubramanian and Kraus to evaluate $T_{\mu\nu}$ associated with a gravitating system in asymptotically AdS spacetime (Balasubramanian & Kraus, 1999; Liu, Lü & Pope, 2014). For the spacetime manifold $\mathcal{M}$ with a time-like boundary $\partial\mathcal{M}$, we define n^μ to be the outward-pointing normal vector to $\partial\mathcal{M}$. Then the induced metric on the boundary is given by

$$h_{\mu\nu} = g_{\mu\nu} - n_\mu n_\nu,$$

and acts as a projection tensor onto $\partial\mathcal{M}$. The extrinsic curvature on the boundary $\partial\mathcal{M}$ is given by

$$K_{\mu\nu} = -\nabla_{(\mu} n_{\nu)}. \tag{2.36}$$

By forming the trace of the extrinsic curvature $K = h^{\mu\nu} K_{\mu\nu}$, we can write the Lagrangian density of the boundary as

$$\mathcal{L}_{\text{surf}} = -\frac{1}{8\pi G}\sqrt{-h}\, K, \tag{2.37}$$

which is the standard Gibbons-Hawking surface term (Gibbons & Hawking, 1977b). However, the energy-momentum tensor that is derived from $\mathcal{L}_{\text{surf}}$ diverges as the boundary is taken to infinity. The solution to this problem is known to be adding counterterms to the action (Emparan, Johnson & Myers, 1999; Myers, 1999). In the case of 4D AdS spacetime, the Lagrangian density of counterterms is

$$\mathcal{L}_{\text{ct}} = \frac{1}{16\pi G}\sqrt{-h}\left[-\frac{4}{\ell} - \ell\mathcal{R}\right], \tag{2.38}$$

where $\mathcal{R}$ is the Ricci tensor of the boundary metric $h_{\mu\nu}$. We should consider boundary term analogous to standard Gibbons-Hawking surface term for the Proca field Y^μ as well

$$\mathcal{L}^Y_{\rm surf} = \frac{\gamma}{8\pi G}\sqrt{-h}\, n^\mu Y_{\mu\nu} Y^\nu. \tag{2.39}$$

To cancel the divergences due to presence of Proca field, The following counterterms are proposed

$$\mathcal{L}^Y_{\rm ct} = -\frac{e_1}{16\pi G\ell}\sqrt{-h}\, Y^\mu Y_\mu. \tag{2.40}$$

The parameters γ and e_1 are currently free; however, they will later be related by imposing the condition of a finite mass. Now, varying the action

$$S = \int_{\partial\mathcal{M}} \left(\mathcal{L}_{\rm surf} + \mathcal{L}_{\rm ct} + \mathcal{L}^Y_{\rm surf} + \mathcal{L}^Y_{\rm ct}\right) d^3x, \tag{2.41}$$

with respect to boundary metric $h_{\mu\nu}$ defines the energy-momentum

$$T_{\alpha\beta} = -\frac{2}{\sqrt{-h}}\frac{\delta S}{\delta h^{\alpha\beta}}, \tag{2.42}$$

which evaluates to

$$\begin{aligned} T_{\alpha\beta} \;=\; & \frac{1}{8\pi G}\Big[-K h_{\alpha\beta} + K_{\alpha\beta} - \frac{2}{\ell}h_{\alpha\beta} + \ell\left(\mathcal{R}_{\alpha\beta} - \frac{1}{2}\mathcal{R} h_{\alpha\beta}\right) \\ & -\frac{1}{2}F_{\mu\nu}A^\nu n^\mu n_\alpha n_\beta + \left(\gamma n^\mu F_{\mu\nu}A^\nu - \frac{1}{2}e_1 l^{-1} A_\alpha A_\beta\right) h^{\alpha\beta} \\ & -2\gamma n^\mu F_{\mu(\alpha}A_{\beta)} + e_1 l^{-1} A_\alpha A_\beta\Big] \end{aligned} \tag{2.43}$$

Substituting boundary metric and the normal vector

$$h_{\mu\nu} = \mathrm{diag}(-h(r), r^2, r^2\sin^2\theta), \qquad n^\mu\partial_\mu = \sqrt{f(r)}\,\frac{\partial}{\partial r}, \tag{2.44}$$

into (2.43), we obtain the T_{tt} component as

$$T_{tt} = \frac{1}{8\pi G}\left[-\frac{2\sqrt{f(r)}\,h(r)}{r} + 2\ell^{-1}h(r) + \frac{\ell h(r)}{r^2} - \alpha\sqrt{f(r)}\,\psi' + \frac{1}{2}\ell\, h(r)\,\psi'^2\right]. \tag{2.45}$$

Integrating T_{tt} over the spatial boundary of the boundary metric $h_{\mu\nu}$ leads to the

following expression for mass

$$M=\frac{1}{2}\Big\{-m_2+q_1q_2\left[\gamma\sigma+\frac{1}{3}(1-\sigma)(\sigma+4)\right]\Big\}, \tag{2.46}$$

where $e_1=(1-\sigma)(1-\gamma)$ is chosen to obtain a finite mass. Now, for simplicity, we take

$$m_2=q_1q_2\left(\gamma\sigma+\frac{1}{3}(1-\sigma)(4+\sigma)\right)-2, \tag{2.47}$$

after normalizing $M=1$. This brings the metric solution (2.32) to its final form

$$\begin{aligned} f(\hat{r}) &= 1+\frac{\hat{r}^2}{l^2}+\frac{(1-\sigma)q_1^2}{4\hat{r}^{1-\sigma}}+\frac{-12+q_1q_2\left(7+6(\gamma-1)\sigma-\sigma^2\right)}{6\hat{r}}, \\ h(\hat{r}) &= 1+\frac{\hat{r}^2}{l^2}+\frac{(1-\sigma)q_1^2}{(3-\sigma)\hat{r}^{1-\sigma}}+\frac{q_1q_2\left(\gamma\sigma+\frac{1}{3}(1-\sigma)(4+\sigma)\right)-2}{\hat{r}}, \end{aligned} \tag{2.48}$$

after using the relations in (2.33) and (2.47). For small $\hat{r}$ namely when $\hat{r}\ll l$, the term $\frac{\hat{r}^2}{l^2}$, coming from AdS background, is negligible and can be dropped. Here, one recalls that $\hat{r}=\kappa^{-1/2}r$ is the dimensionless radius. To simplify the notation, here on we drop hats on parameters namely we use r, M_Y and ϕ to mean $\hat{r}$, $\hat{M}_Y$ and $\hat{\phi}$. We also set $\gamma=1$.

2.3.2 Horizon Structure

In order to study the horizon structure, first we need to find the allowed range of parameters. We find it by setting the condition $0<h(r)<1$. Fig 2.1 shows this region for $\sigma=0.8$. The blue region shows where $h(r)>0$ and on the blue borders $h(r)=0$. In the orange region $h(r)<1$ and on its borders $h(r)=1$. The intersection of these two regions is where $0<h(r)<1$, and we chose the value of q_1 and q_2 from this region.

The Killing horizon and event horizon are located at the value of r for which $h(r)=0$ and $f(r)=0$, respectively. Since the roots of the metric functions cannot be obtained analytically, we illustrate both horizons numerically in Fig 2.2. The solid lines represent the Killing horizon for selected values of the parameters, while the dashed lines show the corresponding event horizons for the same configurations. As expected, the Killing horizon is always hidden behind the event horizon. The separation between these two horizons increases with the Proca charge q_1, while in

the case $q_1 = 0$ the Killing and event horizons coincide — consistent with standard GR solutions.

In the following, We focus on how the Killing horizon radius depends on the values of parameters, since for the purpose of this thesis, $h(r)$ is more relevant. Fig 2.3 shows how it varies according to the parameters q_1 and q_2, When q_1 and q_2 both increase or decrease, the horizon radius decreases, but when one of q_1 or q_2 increases and the other one decreases, the horizon radius increases. We see in both plots when $q_1 = 0$, the horizon radius equals 2, which corresponds to the Schwarzschild case as we expected. It is also visible by setting $q_1 = 0$ in equation (2.48), when $\hat{r} \ll l$. In Fig 2.4, we can see how the horizon radius varies with respect to σ. In all cases, horizon radius increases as σ increases except the case of $q_1 = 0$, which represents the horizon radius for Schwarzschild black holes. Fig 2.5 shows that horizon radius decreases as q_1 or q_2 increases for selected values of σ. The lines intersect where $q_1 = 0$ in the right plot, but they descend and spread as q_1 grows.

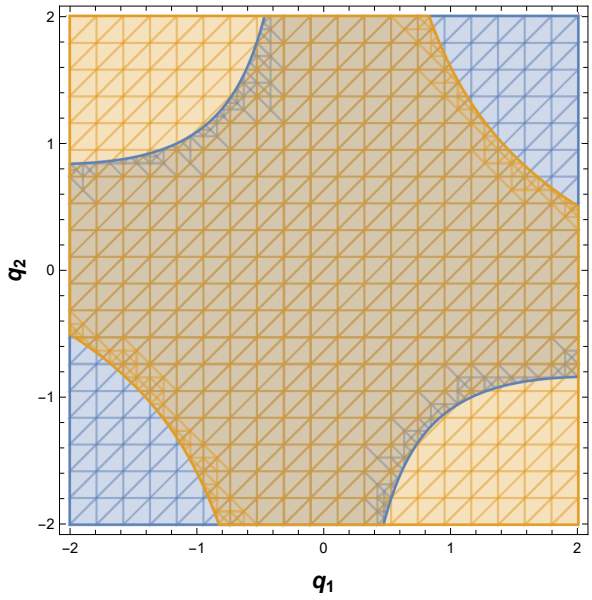

Figure 2.1 The allowed region for choosing the values of the parameters q_1 and q_2. The blue region is where $h(r) > 0$ and the orange region is where $h(r) < 1$. The values of q_1 and q_2 should be chosen from the intersection of these two regions. The values of γ and σ have been set to 1 and 0.8, respectively.

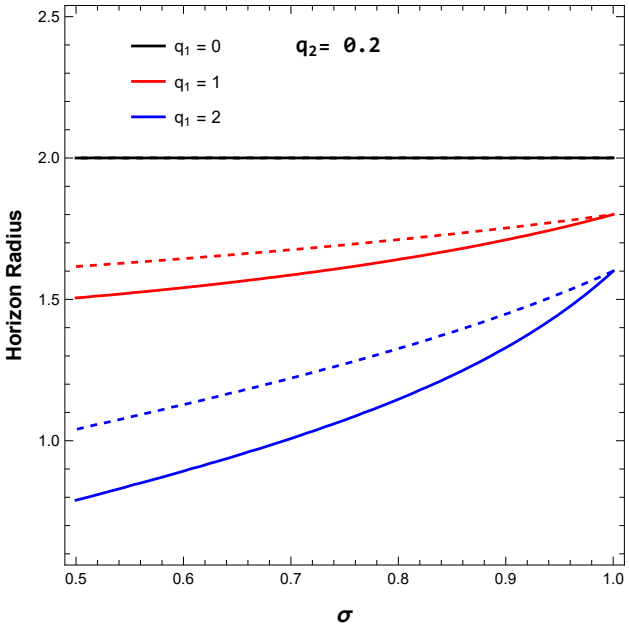

Figure 2.2 Killing horizon and event horizon separation. Solid (dashed) lines correspond to Killing (event) horizon.

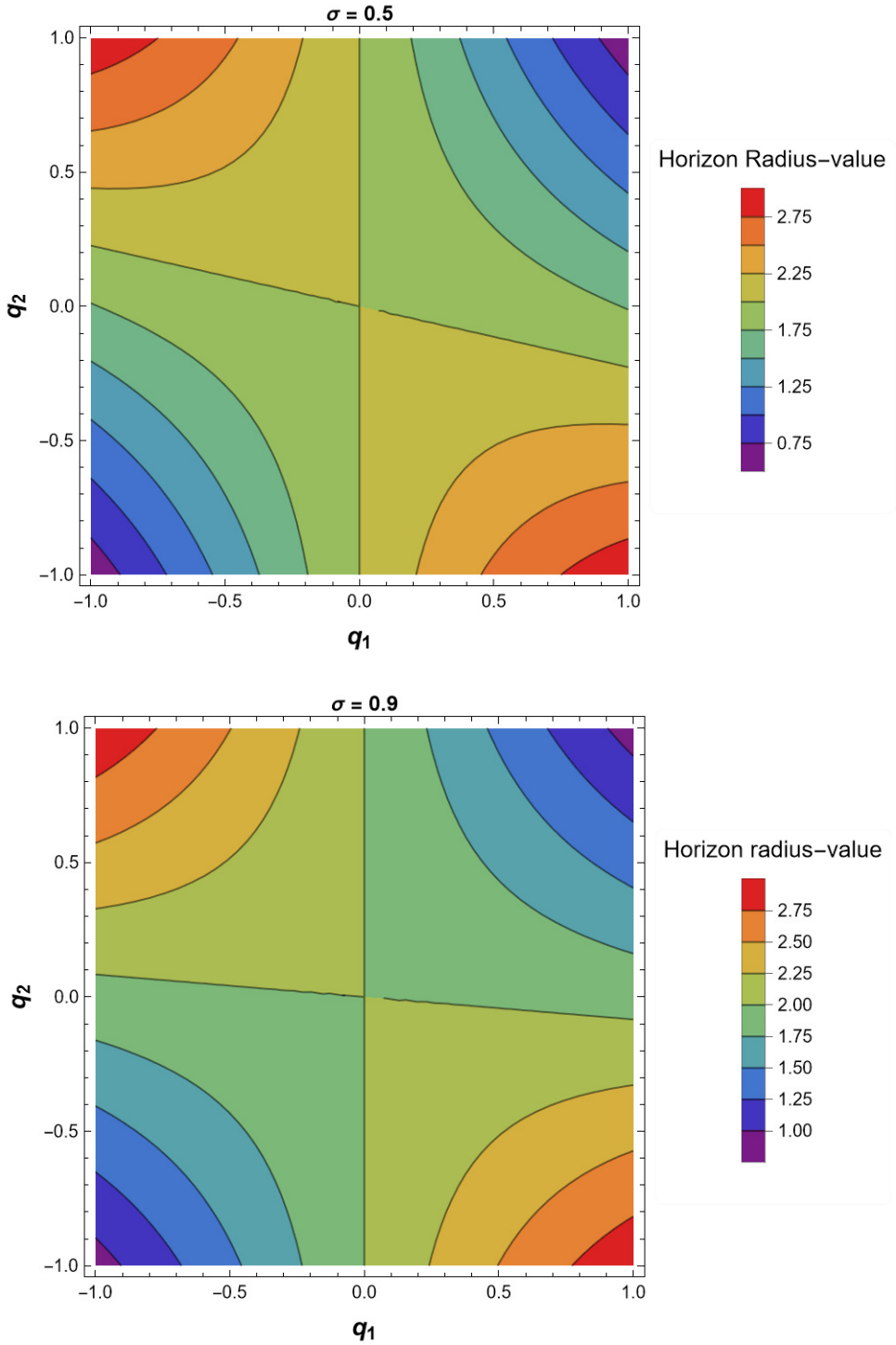

Figure 2.3 The dependence of horizon radius on q_1 and q_2 for two values of $\sigma = 0.5$ and $\sigma = 0.9$.

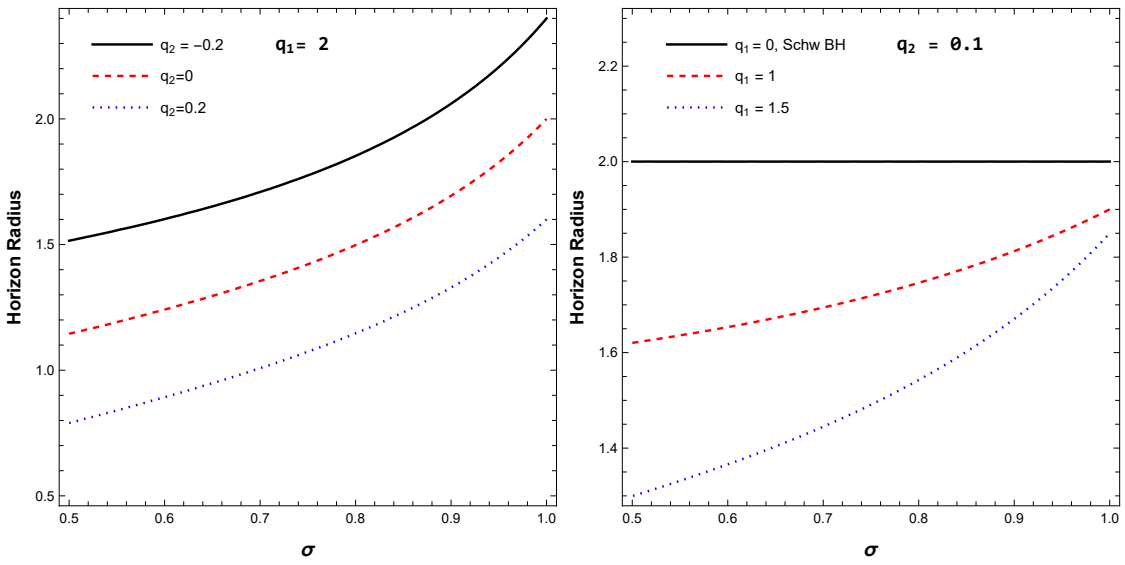

Figure 2.4 Variation of horizon radius with increase of the parameter σ for selected values of q_1 and q_2. In the left plot q_1 is fixed and q_2 takes three different values while in the right plot, q_2 is fixed and q_1 takes three different values. If $q_1 \to 0$, the radius of horizon is the same as the horizon of Schwarzschild BH.

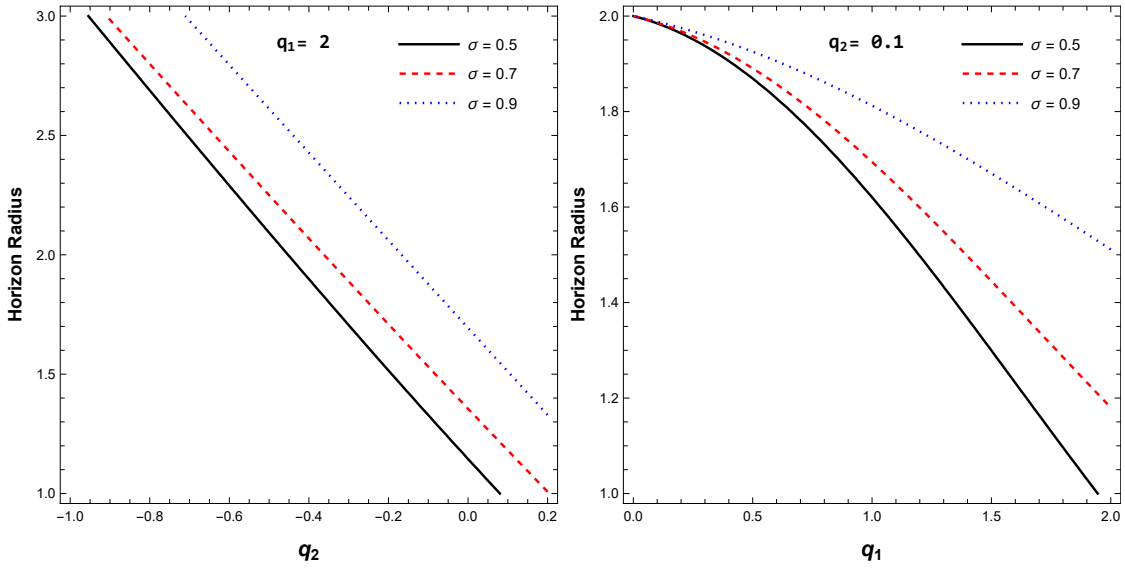

Figure 2.5 The dependence of horizon radius on q_1 and q_2 for three values of σ. The solid black lines, dashed red lines and dotted green lines correspond to $\sigma = 0.5$, $\sigma = 0.7$ and $\sigma = 0.9$, respectively. In the left plot q_1 is fixed and in the right plot q_2 is fixed.

2.3.3 Curvature Invariants

To study the geometric structure of the EMPG spacetime around Einstein–Geometric Proca AdS black holes, we compute the relevant curvature invariants: The Kretschmann scalar (KS) $R_{\mu\nu\sigma\rho}R^{\mu\nu\sigma\rho}$ and the Ricci-squared (RS) scalar $R_{\mu\nu}R^{\mu\nu}$. They both possess lengthy expressions as invariant functions of r, σ, q_1 and q_2. It is clear from (2.48) that, for $q_1 = 0$, the geometry reduces to Schwarzschild geometry namely $f(r) = h(r) = 1 - 2/r$ with a horizon at $r = 2$. In this sense, to reveal the geometry of the EMPG black hole near the Schwarzschild limit we expand the KS and RS scalars around $q_1 = 0$ up to quadratic order to find

$$
\begin{aligned}
R_{\mu\nu\sigma\rho}R^{\mu\nu\sigma\rho} = \frac{48}{r^6} + \frac{q_1}{36r^6(r-2)^4}\Bigg(& -\frac{1}{\sigma-3}\Big[72q_1 r^{\sigma}(r-2)^2(\sigma-1)\,(72 \\
& - 98\sigma + 22\sigma^2 + r^2(\sigma-3)(5\sigma-7) + r(\sigma(94-21\sigma)\sigma - 77))\Big] \\
& + q_1 q_2^2\Big[192(\sigma^2-7)^2 + 6r^4(5\sigma^4 - 46\sigma^2 + 113) - 16\hat{r}^3(8\sigma^4 - 103\sigma^2 + 311) \\
& + r^2(241\sigma^4 - 4130\sigma^2 + 14257) - 16r(19\sigma^4 - 326\sigma^2 + 1171)\Big] + 48q_2(r-2)^2 \\
& \times\Big[r(9r(\sigma^2-5) - 29\sigma^2 + 173) + 24(\sigma^2-7)\Big]\Bigg),
\end{aligned}
\tag{2.49}
$$

and

$$
R_{\mu\nu}R^{\mu\nu} = \frac{q_1^2 q_2^2(9 + r(3r-10))(\sigma^2-1)^2}{72(r-2)^4 r^4}. \tag{2.50}
$$

These invariants exemplify the KS and RS scalars near the physically-interesting domain of the Schwarzschild black hole. The KS scalar, as revealed by (2.49), fully agrees with the Schwarzschild limit at the zeroth order in q_1. The RS scalar, on the other hand, vanishes up to the quadratic order q_1, in accordance with the Schwarzschild limit. In general, KS and RS behave differently in different geometries. In Schwarzschild solution, for instance, the spacetime is Ricci-flat and KS remains as the indicator of the black hole singularity. In the EMPG this picture changes as a funtion of q_1 (and other parameters).

From hereon, we want to dwell on the singularity structure of the black hole by analyzing the KS in detail. The EMPG black hole develops two true singularities, one at the origin $r = 0$ and the other at the killing horizon $r = r_H$. We call them primary and secondary singularities, respectively. (In the literature singularities at different r values have already been discussed for the KS for the 5-dimensional Schwarzschild-AdS spacetimes (Seahra, 2005), for the brane solutions of supergravity theory (Peet, 2000) and for spherically-symmetric solutions of general relativity with

scalar fields (Stashko & Zhdanov, 2021).) Near the Schwarzschild limit $q_1 = 0$, the KS expression in (2.49) shows explicitly that the secondary singularity occurs at $r = 2$, which is the event horizon of the Schwarzschild black hole. The primary singularity remains just as in the Schwarzschild case. The secondary singularity, however, changes with changing parameters. Indeed, as we illustrate in Fig. 2.6, the secondary singularity varies with different sets of q_1 and q_2. (Setting $\sigma = 0$ and $\gamma = 1$).

It is worth nothing that the secondary singularity is a signature of the Proca field. Indeed, as $\sigma \to 1$ (for which $M_Y \to 0$) it is found that the KS reduces to $(\mathrm{KS})_{EMPG} = (\mathrm{KS})_{Sch} + (12q_1q_2(q_1q_2 - 4))/r^6$ having a sole singularity at the origin just like Schwarzschild case (with a q_1 and q_2 dependent residues, though). In this limit one recovers the electromagnetism-like geometric vector field. It is in this sense that the secondary singularity at the horizon $r = r_H$ is a **direct signature of the Proca field**. In fact, the plots in Fig. 2.6 illustrate $\sigma = 0$, a point far from the electromagnetism-like limit of $\sigma = 1$. Basically, sensitivity of the EMPG black hole on the parameters σ, q_1 and q_2 introduce a certain form of "hair". It turns out the EMPG black hole possesses structures beyond the Schwarzschild case.

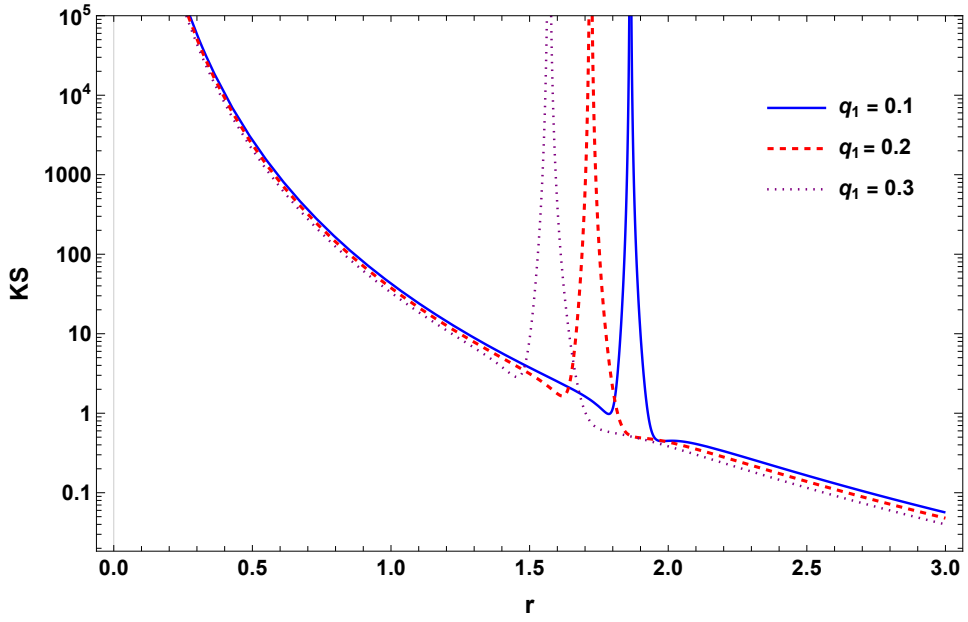

Figure 2.6 Variation of the Kretschmann scalar (KS) of the EMPG black hole with the radial distance r for $q_2 = 1$ and different values of q_1 with $\sigma = 0$ and $\gamma = 1$. The KS is seen to develop two singularities, one at the origin $r = 0$ (independent of parameters) and the other at the horizon $r = r_H$ (dependent of the parameters).

2.3.4 The Stability of EMPG Black Hole

The stability of the EMPG black hole is another point to dwell on. In the literature, stability conditions for the spherically symmetric solutions of the extended gravity theories have been discussed in (Addazi, Capozziello & Odintsov, 2021; Sebastiani, Momeni, Myrzakulov & Odintsov, 2013). The EMPG black hole admits the solution

$$h(r) = f(r) = 1 - \frac{2M_{BH}}{r} - \frac{\Lambda r^2}{3}, \tag{2.51}$$

as follows from the metric potentials in (2.32) and (2.33) after ignoring the matter contribution by taking $\sigma = 1$ and after setting $m_2 = -2M_{BH}$. As was shown in (Addazi et al., 2021; Sebastiani et al., 2013), near the extremal limit one is led to the Nariai black hole metric

$$ds^2 = e^{2\rho}(-d\tau^2 + dx^2) + e^{-2\phi}d\Omega^2, \tag{2.52}$$

in which

$$e^{2\rho} = -\frac{1}{\Lambda \cos^2\tau}, \;\; e^{-2\phi} = \frac{1}{\Lambda}, \tag{2.53}$$

where $\tau = \arccos(\cosh t)^{-1}$. Clearly, $-\infty < t < \infty$ corresponds to $-\pi/2 < \tau < \pi/2$ in the Nariai solution. It is necessary to study especially the perturbations $\delta\phi$ about the Nariai solution to determine stability of its spherically-symmetric structure:

$$\phi = \ln\sqrt{\Lambda} + \delta\phi. \tag{2.54}$$

For $\delta\phi$, the perturbed Einstein field equations give the motion equation

$$\frac{d^2\delta\phi}{dt^2} + \tanh t \frac{d\delta\phi}{dt} - m^2\delta\phi = 0, \tag{2.55}$$

in terms of the cosmological time t and the mass parameter

$$m^2 = \frac{2(2\alpha - 1)}{3\alpha}, \tag{2.56}$$

where the parameter α is set by the curvature sector. It is clear that perturbations remain stable for $0 < \alpha < 1/2$ for which $2\alpha - 1 < 0$. For $f(R)$ gravity is given by (Addazi et al., 2021; Sebastiani et al., 2013)

$$\alpha = \frac{\Lambda f_{RR}(R_0)}{f'(R_0)}, \tag{2.57}$$

at constant curvature $R = R_0 = 4\Lambda$. In this expression f_R denotes derivative of f with respect to R and f' denotes derivative with respect to the radial coordinate r. At large times $t \to \infty$ $\tanh t \to 1$ and the perturbation in (2.55) behave as

$$\delta\phi = \phi_0 \; e^{\lambda_g t}, \tag{2.58}$$

with the initial value ϕ_0 and the Lyapunov exponent $\lambda_g = (-1 \pm \sqrt{1+4m^2})/2$.

The EMPG model is an $f(R) = R - 2\Lambda$ theory. It is linear and it has therefore

$$\alpha = 0, \tag{2.59}$$

as follows from (2.57). This α value is at the edge of the stability interval. It requires $m^2 \to -\infty$ and this corresponds to a fully stable perturbation as follows from (2.55). The corresponding Lyapunov exponent implies periodic time-dependence for $\delta\phi$ and this dependence ensures stability.

This stable solution of the perturbation shows that there arise no metric instabilities in the EMPG black hole (in the absence of matter). The perturbation does not diverge. It is in this regard that the EMPG model is devoid of any metric instabilities.

It is known that the critical impact parameter b_C and the critical photon-trajectory are determined by the time-varying horizon radius which depends on the Lyapunov exponent as (Sebastiani et al., 2013)

$$b_C \simeq \sqrt{3} r_{ph} = \sqrt{3}(3/2) r_H(t) = \sqrt{3}(3/2) r_H(0) e^{\lambda_g t}, \tag{2.60}$$

so that for the EMPG model one expects no instability in the photon trajectory. Indeed, as expected from the imaginary value of λ_g for $\alpha = 0$, the photon radius shows small variations about the EMPG horizon radius $r_H(0)$.

The black holes can be destabilized also by non-minimal couplings of the Proca field (Garcia-Saenz, Held & Zhang, 2021). This has been shown explicitly for the Schwarzschild solution in the presence of the non-minimally coupled Proca fields. But the EMPG model is a minimal Proca model (with no higher-order couplings to the self and to the curvature), and no instability is expected in this sense.

3. OPTICAL PROPERTIES OF THE EMPG BLACK HOLES

In this chapter, we study photon motion around a compact object in the EMGP model to investigate the optical properties of EMPG black holes both in vacuum and in the presence of a plasma environment. We analyze how the photon sphere and shadow radius depend on the model parameters. In the final part, we constrain the black hole charges q_1 and q_2 using observational data of black hole shadows. Before presenting the calculations, we review the main concepts of this chapter briefly, here.

Naively speaking, a distant observer would detect a dark area in the direction of the black hole, known as the **black hole shadow**. However, due to the curvature and bending of light, the angular size of the shadow differs from what we expect in Euclidean geometry. Fig. 3.1 clarifies this situation. In the left panel, three classes of light rays are shown. Blue rays fall into the black hole and never escape. Red rays escape to infinity after being deflected by the black hole's gravity. The borderline between these cases is formed by the orange rays, which spiral asymptotically toward the **photon sphere**. This is a spherical region where gravity is strong enough to force photons into circular orbits. As shown in the right panel of Fig.3.1, the photon sphere determines the angular size of the shadow. The observed radius of the shadow corresponds to the photon sphere radius plus the light bending, as indicated by the blue arrow (Bisnovatyi-Kogan, Tsupko & Perlick, 2019; Perlick et al., 2015).

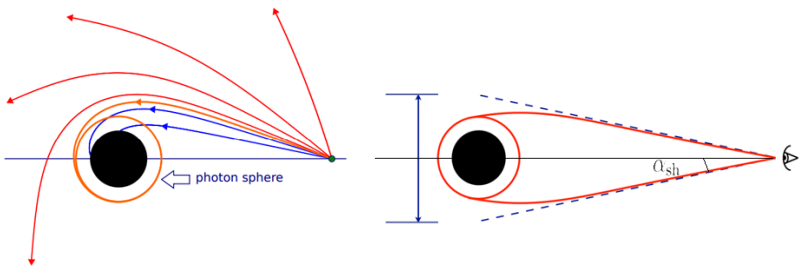

Figure 3.1 Left panel illustrates the formation of the photon sphere and the black hole shadow due to the bending of light. Right panel compares the angular size of the photon sphere and the observed shadow.

Source: Tsupko & Perlick. (2019)

However, the observed bright ring seen by the Event Horizon Telescope (EHT) around Sgr A* — the Milky Way's central black hole — may not be purely gravitational in origin. Instead, it could be influenced by the surrounding plasma, which affects the propagation of light. Therefore, understanding how plasma modifies light trajectories is essential for accurately interpreting the black hole shadow.

3.1 Photon Motion

To begin, we examine the dynamics of photons in the curved spacetime of the EMPG black hole. Since photons are massless and follow null geodesics, their trajectories satisfy the Hamiltonian constraint $\mathcal{H} = 0$. We will use this constraint to determine the photon sphere. The Hamiltonian of the photons reads as

$$\mathcal{H} = \frac{1}{2}\Big[g^{\alpha\beta}p_\alpha p_\beta\Big], \tag{3.1}$$

where p^α is the 4-momentum of the photons. The components of the 4-velocity for the photons in the equatorial plane ($\theta = \pi/2,\ p_\theta = 0$) are given by

$$\dot{t} \equiv \frac{dt}{d\lambda} = \frac{-p_t}{h(r)}, \tag{3.2}$$

$$\dot{r} \equiv \frac{dr}{d\lambda} = p_r f(r), \tag{3.3}$$

$$\dot{\phi} \equiv \frac{d\phi}{d\lambda} = \frac{p_\phi}{r^2}, \tag{3.4}$$

where we used the relationship $\dot{x}^\alpha = \partial\mathcal{H}/\partial p_\alpha$. From Eqs. (3.3) and (3.4), we obtain a governing equation for the phase trajectory of light.

$$\frac{dr}{d\phi} = \frac{r^2 p_r f(r)}{p_\phi}. \tag{3.5}$$

Using the constraint $\mathcal{H} = 0$, one can rewrite the above equation as (Perlick et al., 2015)

$$\frac{dr}{d\phi} = \sqrt{r^2 f(r)}\sqrt{\gamma^2(r)\frac{p_t^2}{p_\phi^2} - 1}, \tag{3.6}$$

where we defined

$$\gamma^2(r) = \frac{r^2}{h(r)}. \tag{3.7}$$

The radius of a circular orbit of light, particularly the one which forms the photon sphere of radius r_{ph}, is determined by solving the following equation (Papnoi & Atamurotov, 2022)

$$\left.\frac{d(\gamma^2(r))}{dr}\right|_{r=r_{ph}} = 0. \tag{3.8}$$

The solution of this equation is found numerically and depicted in Figs. 3.2 and 3.3. The plots for photon sphere radius exhibit exactly the same pattern as the horizon radius, as shown in Figs. 2.4 and 2.5. One may see that photon sphere enlarges as σ increases except the case of $q_1 = 0$, for which the photon sphere radius is $r_{ph} = 3$ and represents Schwarzschild black holes.

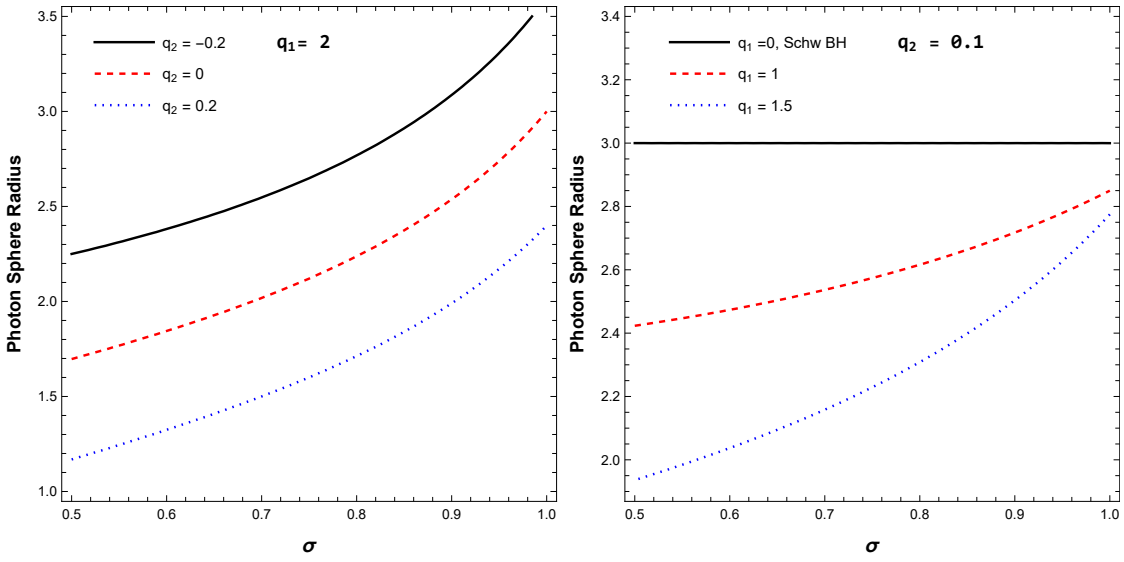

Figure 3.2 Variation of photon sphere radius with increase of the parameter σ, for selected values of q_1 and q_2. In the left plot q_1 is fixed and q_2 takes three different values while in the right plot, q_2 is fixed and q_1 takes three different values. If $q_1 \to 0$, the radius of photon orbit is the same as with Schwarzschild BH's orbit.

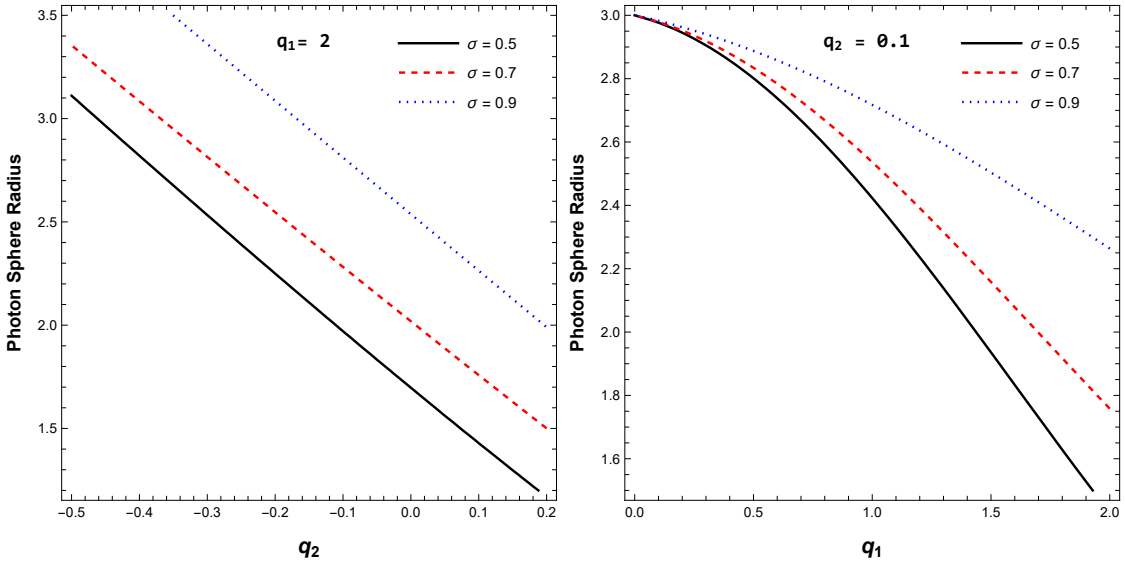

Figure 3.3 The dependence of photon sphere radius on q_1 and q_2 for three values of σ. The solid black lines, dashed red lines and dotted green lines correspond to $\sigma = 0.5$, $\sigma = 0.7$ and $\sigma = 0.9$, respectively. In the left plot q_1 is fixed and in the right plot q_2 is fixed.

3.2 Black Hole Shadow

In this subsection we study the shadow of the BH described by the EMPG spacetime. For the angular radius of the BH shadow α_{sh} shown in Fig.3.1 we explore (Perlick & Tsupko, 2022)

$$\sin^2 \alpha_{sh} = \frac{\gamma(r_{ph})^2}{\gamma(r_{obs})^2}, \tag{3.9}$$

which comes from the elementary trigonometry and

$$\gamma(r)^2 = \frac{g_{22}}{g_{00}} = \frac{r^2}{h(r)}. \tag{3.10}$$

r_{obs} is observer distance and r_{ph} is already introduced in the previous subsection as the photon sphere radius. The Observer distance is very large but finite, and it has the value $r_{obs} = D = 8.3$ kpc for the Sgr A*(Akiyamaet al. , 2022) or $r_{obs} = D = 16.8$ Mpc for the M87*(Akiyamaet al. , 2019a).

Now we combine Eqs. (3.9) and (3.10), and for an observer the Eq. (3.9) takes the following form

$$\sin^2 \alpha_{sh} = \frac{r_{ph}^2}{h(r_{ph})} \frac{h(r_{obs})}{r_{obs}^2}. \tag{3.11}$$

One can find the radius of BH shadow for an observer at large distance using Eq. (3.11) as (Perlick & Tsupko, 2022)

$$R_{sh} \simeq r_{obs} \sin \alpha_{sh} \simeq \frac{r_{ph}}{\sqrt{h(r_{ph})}} \sqrt{h(r_{obs})}. \tag{3.12}$$

Fig. 3.4 shows how the shadow radius changes with respect to σ for different values of q_1 and q_2. Increasing the value of q_1 or q_2, when one of them held fixed, decreases the shadow size. It is also worth mentioning that if we reverse the signs of q_1 and q_2 at the same time in Figs. 2.4, 3.2 and 3.4, we get exactly the same plots. This is because in the equation (2.48), in the lapse function, we have q_1^2 in the second term and the product $q_1 q_2$ in the third term. Then, when q_1 and q_2 are both positive or negative, we get the same result. When they have opposite signs, negative q_1 and positive q_2 give the same result as a positive q_1 and negative q_2 provided that $|q_1|$ and $|q_2|$ remain unchanged. Fig 3.5 shows the change of shadow size according to q_1 and q_2. Again, in the right plot, we see the shadow size of Schwarzschild black holes where the lines intersect at $q_1 = 0$.

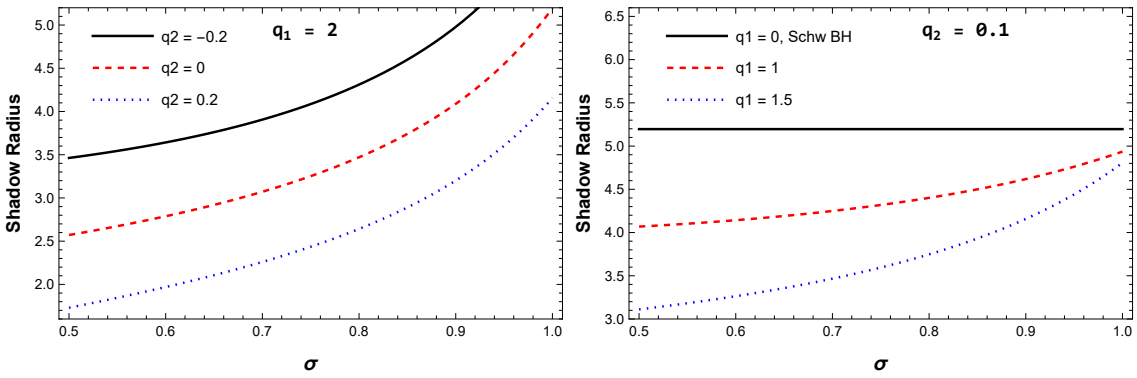

Figure 3.4 Variation of shadow radius with increase of the parameter σ, for selected values of q_1 and q_2. In the left plot q_1 is fixed and q_2 takes three different values while in the right plot, q_2 is fixed and q_1 takes three different values. If $q_1 \to 0$, the radius of BH shadow is the same as with Schwarzschild BH.

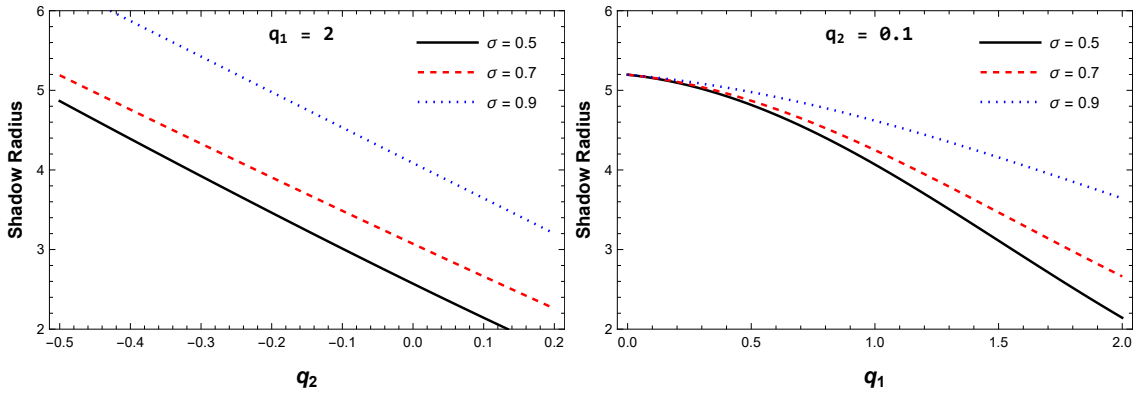

Figure 3.5 The dependence of shadow radius on q_1 and q_2 for three values of σ. The solid black lines, dashed red lines and dotted green lines correspond to $\sigma = 0.5$, $\sigma = 0.7$ and $\sigma = 0.9$, respectively. In the left plot q_1 is fixed and in the right plot q_2 is fixed.

3.3 Photon Motion in Plasma Medium

In this subsection we investigate the effect of a plasma environment on the photon motion around the BH. The Hamiltonian (3.1) for a photon is modified in the presence of a plasma and can be written as (Atamurotov et al., 2021; Badía & Eiroa, 2021; Perlick et al., 2015; Synge, 1960)

$$\mathcal{H} = \frac{1}{2}\left[g^{\alpha\beta}p_\alpha p_\beta + \omega_p^2\right], \tag{3.13}$$

where $\omega_p = \frac{4\pi e^2}{m_e}N_e(x)$ is the plasma frequency (Perlick et al., 2015). N_e is the number density of electrons, e and m_e are the charge and mass of electron, respectively.

The components of the four velocity for the photons and the governing equation for the phase trajectory of light are the same as equations (3.2) to (3.6) with the new $\gamma^2(r)$ modified as (Atamurotov et al., 2021; Perlick et al., 2015)

$$\gamma^2(r) = r^2\left(\frac{1}{h(r)} - \frac{\omega_p^2}{\omega_0^2}\right), \tag{3.14}$$

where $\omega_0 = -p_t$ is the photon frequency as seen by a distant observer. Then photon sphere is defined as a solution of the following equation

$$\frac{d}{dr}[\gamma^2(r)]\Big|_{r=r_{ph}} = 0. \tag{3.15}$$

Here we consider two cases: uniform plasma and non-uniform plasma. Uniform

plasma is defined as $\omega_p^2/\omega_0^2 = \text{constant}$. For the non-uniform plasma, for the simplicity, we choose the following radial dependence of plasma frequency (Atamurotov et al., 2021; Rogers, 2015):

$$\omega_p^2(r) = \frac{z_0}{r}. \tag{3.16}$$

z_0 is a free constant parameter (Atamurotov et al., 2021; Rogers, 2015). Fig 3.6 shows the photon sphere size for uniform and non-uniform plasma. In both cases (left panels) photon sphere grows as ω_p^2/ω_0^2 or z_0/ω_0^2 grow but the effect of ω_p^2/ω_0^2 on increasing the size of photon sphere in uniform case is stronger than the effect of z_0/ω_0^2 in non-uniform case. The right panels show the effect of q_1 on the photon sphere size in the plasma environment. In contrast to the vacuum case, photon sphere enlarges as q_1 grows and becomes bigger than photon sphere of the Schwarzschild black holes.

3.4 Black Hole Shadow in Plasma Medium

Now we investigate the radius of the shadow of the BH with the EMPG model in a plasma medium. Using Eq. (3.14), the shadow radius $R_{\rm sh}$ given by Eq. (3.12) is substituted by the following (Atamurotov et al., 2021; Perlick et al., 2015)

$$R_{\rm sh} \simeq \sqrt{r_{\rm ph}^2\left[\frac{1}{h(r_{\rm ph})} - \frac{\omega_p^2(r_{\rm ph})}{\omega_0^2}\right]h(r_{obs})}. \tag{3.17}$$

In the vacuum case $\omega_{\rm p}(r) \equiv 0$, we recover the shadow radius of the black hole in the EMGP model without a plasma medium, as given by Eq. (3.12).

Fig 3.7 shows the shadow size for uniform and non-uniform plasma. In the left panels, we see the shadow size decreases as the plasma frequency increases, but we have seen that, for the same values of parameters, the photon sphere grows as plasma frequency grows in Figs 3.6. In other words, plasma brings photon sphere and shadow close to each other. Again one can see the effect of q_1 on the shadow radius in the right panels and compare our result with the Schwarzschild case, which is shown in the figure coresponding to the case of $q_1 = 0$. It is also worth mentioning that for all the cases we studied till now, photon sphere and shadow had the same

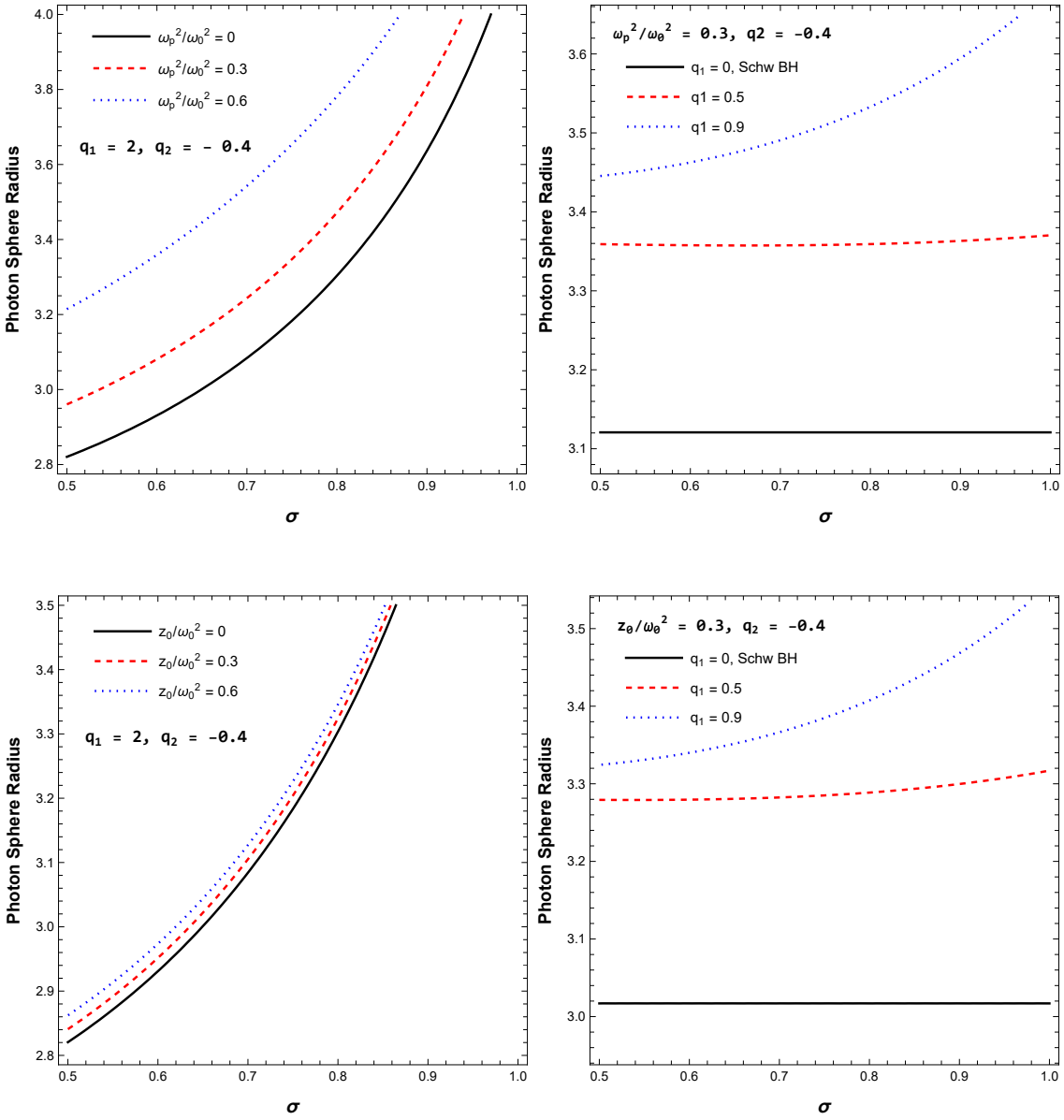

Figure 3.6 The dependence of photon sphere radius on σ for selected values of q_1 and q_2 in uniform (upper panels) and non-uniform (lower panels) plasma. In the left panels q_1 and q_2 are fixed while plasma frequency is changing. In the right panels, plasma frequency and q_2 are fixed but q_1 is changing. If $q_1 \to 0$, the radius of photon orbit is the same as with Schwarzschild BH case.

behaviour with respect to σ, for the same parameter choices.

Fig. 3.8 compares photon sphere and shadow for three cases: vacuum, uniform plasma, and non-uniform plasma. Here we can clearly see that plasma increases the photon sphere radius but decreases the shadow radius.

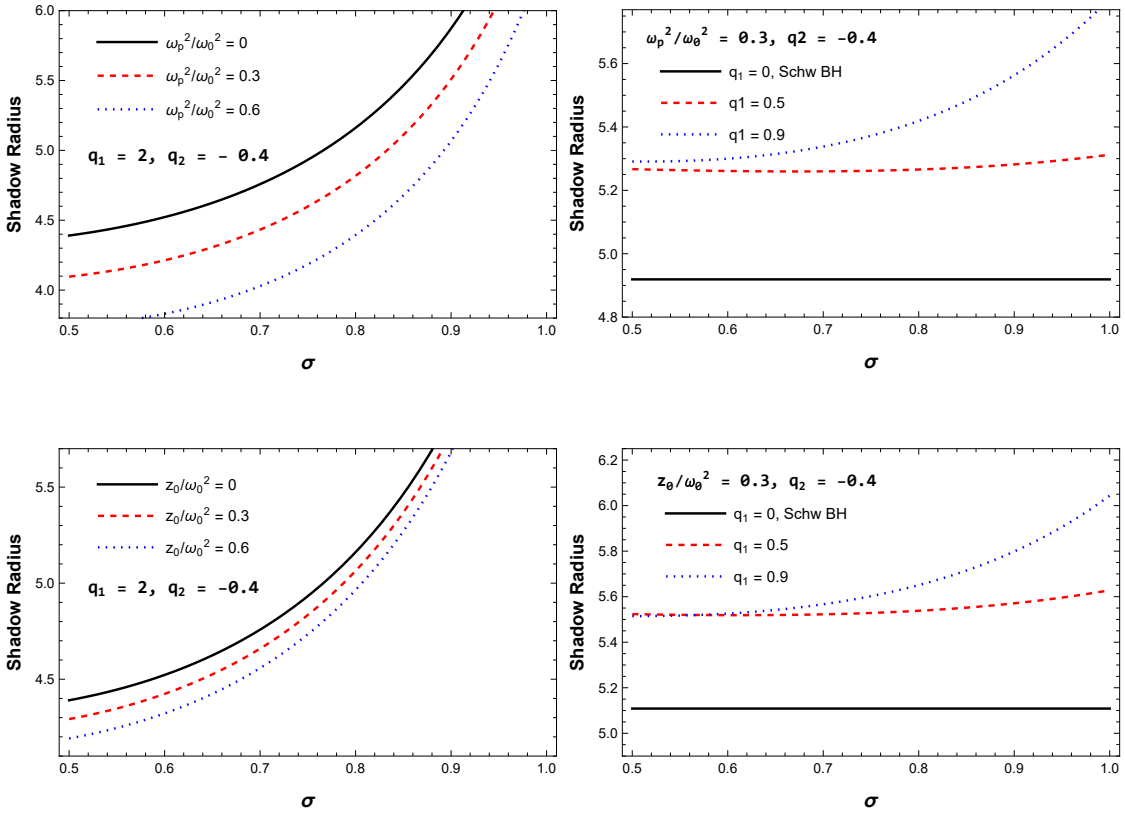

Figure 3.7 The dependence of shadow radius on σ for selected values of q_1 and q_2 in uniform (upper panels) and non-uniform (lower panels) plasma. In the left panels q_1 and q_2 are fixed while plasma frequency is changing. In the right panels, plasma frequency and q_2 are fixed but q_1 is changing. If $q_1 \to 0$, the radius of BH shadow is the same as with Schwarzschild BH case.

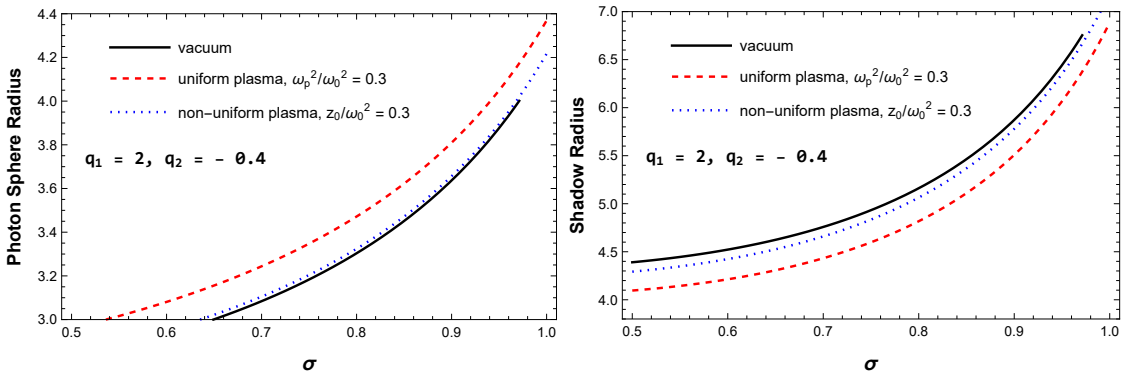

Figure 3.8 Comparing photon sphere and shadow radius for vacuum, uniform plasma, and non-uniform plasma. The solid black lines, dashed red lines and dotted blue lines correspond to vacuum, uniform plasma, and non-uniform plasma cases, respectively.

3.5 Astrophysical Constraints from the EHT Observations

In general, a BH shadow has two observable parameters: *(i)* shadow radius, and *(ii)* its distortion from the circle shape. Observations of the supermassive black holes (SMBHs) M87* and Sgr A* have revealed that their shadow shape are almost circular with a very small distortion parameter (with about $1-5$ % variation). Also revealed is that shadows of both SMBHs have some common features like for example shadow's center has some brightness depression and both are nearly-circular rings. As a result, the EHT collaboration has determined sizes of these BHs by assuming ring-shaped structures. Here, in this section, we will explore potential constraints on the Proca field parameters using the Hioki& Maeda method and the EHT observations of the shadows cast by SMBHs M87* and Sgr A*. Throughout our analysis will be based on the Einstein-geometric Proca BH solution.

In Figs. 3.9 and 3.10, depicted are the constraints on possible values of the parameters q_1 and q_2 (between red-dashed and blue solid curves) using the observational angular size of SMBHs M87* and Sgr A* for $\sigma = 0.5$ and $\sigma \to 1$. It is seen from the figure that the constrained range increases slightly with the increase in the angular size. The ranges of q_1 and q_2 considerably increase in the presence of a uniformly distributed plasma with the frequency ratio $\omega_p/\omega_0 = \sqrt{0.3}$ (corresponding to a plasma frequency of about 127 GHz). In the limit $\sigma \to 0$, constrained values of q_1 and q_2 obey power-law behavior: $q_1 q_2 = \text{const}$, where the constant depends on the plasma frequency and the angular size. It is seen from both figures that the value of the constant decreases as the plasma frequency and the angular size increase. However, in $\sigma = 0.5$ case, q_1 and q_2 parameters have a complicated relationship depending on the size and plasma frequency. Moreover, in this case, the constrained ranges of q_1 and q_2 parameters for M87* are bigger than that which for Sgr A*, due to its large mass.

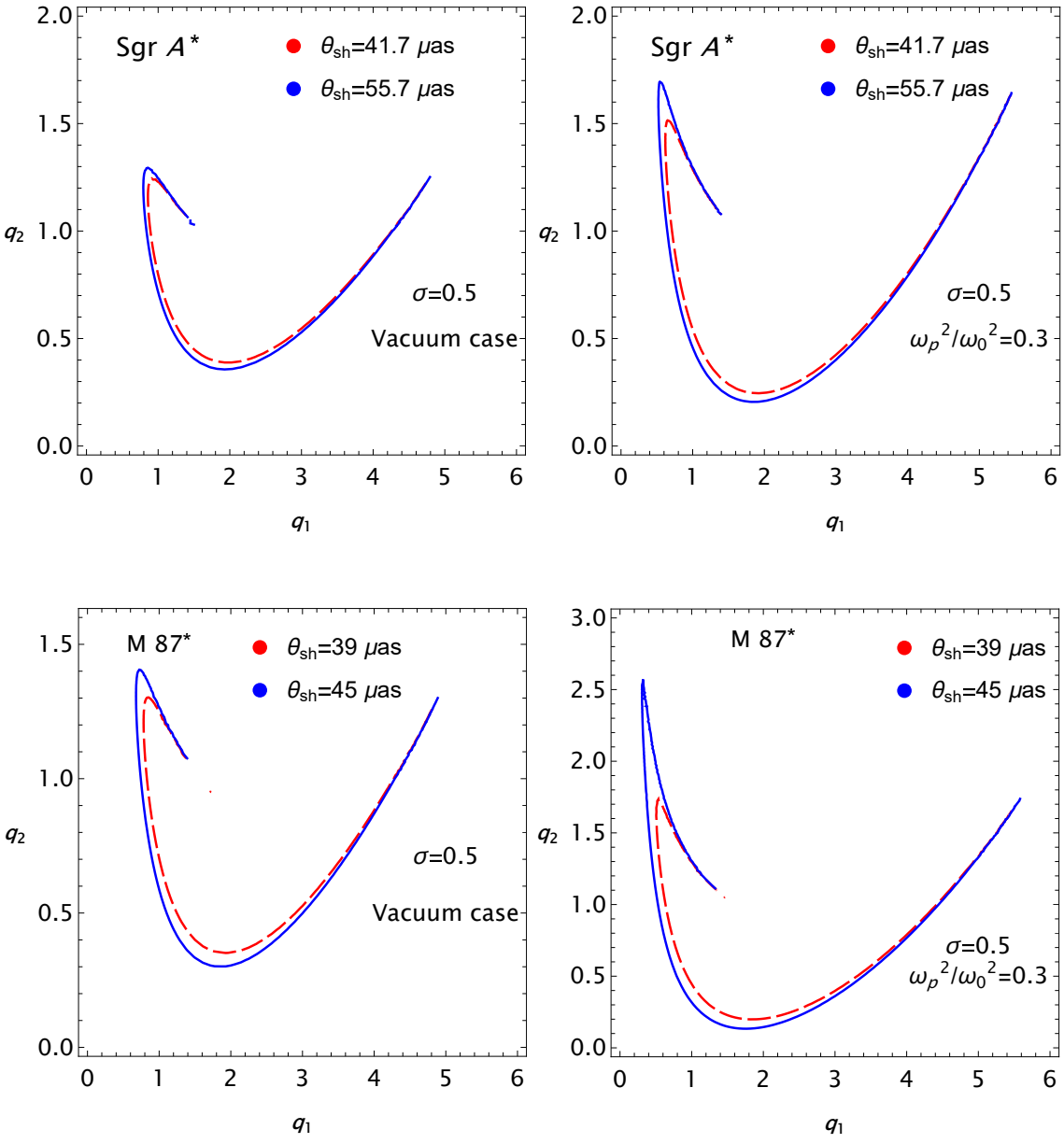

Figure 3.9 Constraints on possible values of the parameters q_1 and q_2 for $\sigma = 0.5$. Here, we used the observational angular size of SMBHs M87* and SgrA* as $\theta_{sh} = 42 \pm 3\mu$as and $\theta_{sh} = 48.7 \pm 7\mu$as, respectively.

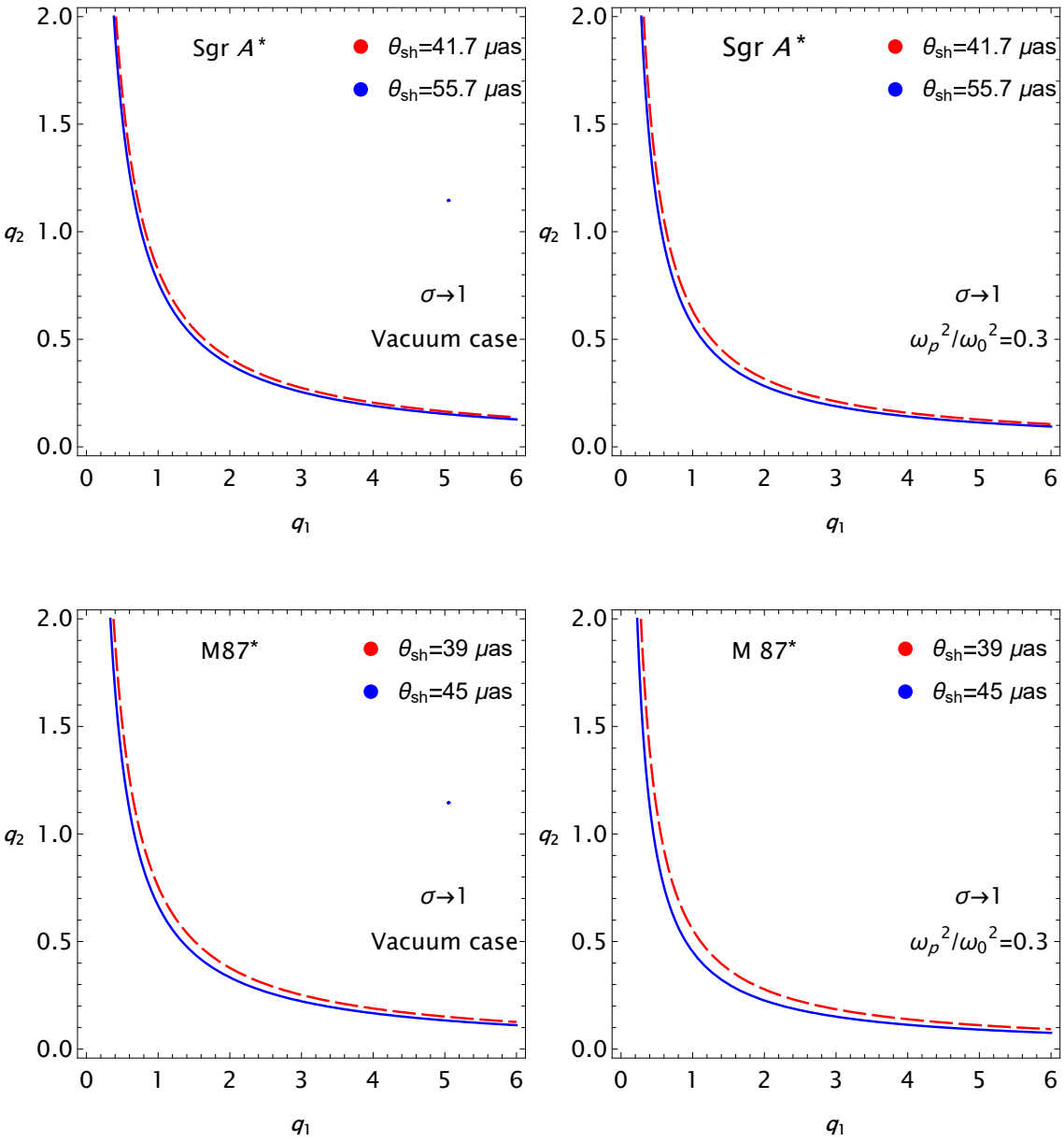

Figure 3.10 The same as Fig. 3.9 but for $\sigma \to 1$.

4. CONSTRAINTS ON EMPG BLACK HOLES FROM QPO DATA

In this chapter, our aim is to further constrain the parameters of the EMPG model using observational data on **quasi-periodic oscillations (QPOs)** from stellar-mass, supermassive, and intermediate-mass black holes. QPOs are observed as narrow, coherent peaks in the X-ray power spectra of accreting black holes and neutron stars. QPOs are believed to originate from orbital motion near the **innermost stable circular orbit (ISCO)** and it is observed that the peaks correspond directly to the fundamental orbital frequencies of test particle near the ISCO (Ingram & Motta, 2020).

We analyze the dynamics of test particles around the Einstein–geometric Proca AdS black hole and determine the location of the ISCO. We then compute the fundamental frequencies associated with small oscillations about circular orbits — namely, the Keplerian (azimuthal), radial, and vertical frequencies. This enables us to compare and constrain the EMPG model parameters using QPO observational data. However, real accretion disks are fluids, and additional effects such as pressure gradients, viscosity, turbulence, and magnetic fields can influence the effective location of characteristic radii and the associated oscillation modes. Our results should therefore be regarded as an idealized first step within the geodesic approximation.

4.1 Particle Motion

To study the motion of massive test particles around EMPG black holes, we begin with the Lagrangian formalism. The Lagrangian for a massive test particle reads as

$$L_p = \frac{1}{2} m g_{\alpha\beta} \dot{x}^\alpha \dot{x}^\beta, \tag{4.1}$$

in which m is the mass of the particle. One finds the conservation laws

$$g_{tt}\dot{t} = -\frac{E}{m}, \quad g_{\phi\phi}\dot{\phi} = \frac{L}{m}, \tag{4.2}$$

in terms of the conserved energy E and conserved angular momentum L of the particle. With the normalization condition for massive particles moving along timelike geodesics

$$g_{tt}\dot{t}^2 + g_{rr}\dot{r}^2 + g_{\theta\theta}\dot{\theta}^2 + g_{\phi\phi}\dot{\phi}^2 = -1, \tag{4.3}$$

we get

$$g_{rr}\dot{r}^2 + g_{\theta\theta}\dot{\theta}^2 = -\left(1 + \frac{E^2}{m^2 g_{tt}} + \frac{L^2}{m^2 g_{\phi\phi}}\right), \tag{4.4}$$

by using the conserved quantities in (4.2). We can rearrange (4.4) as

$$g_{rr}\dot{r}^2 + g_{\theta\theta}\dot{\theta}^2 = -\Pi(r,\theta) \tag{4.5}$$

with

$$\Pi(r,\theta) = 1 + \frac{\mathcal{E}^2}{g_{tt}} + \frac{\mathcal{L}^2}{g_{\phi\phi}} \tag{4.6}$$

where $\mathcal{E}$ and $\mathcal{L}$ are $-E/m$ and L/m, respectively. In the azimuthal $\theta = \pi/2$ plane, the motion in the radial direction obeys the equation

$$g_{rr}\dot{r}^2 = -\Pi(r,\theta_0) = R(r) \tag{4.7}$$

where

$$R(r) = -\frac{1}{g_{tt}}(\mathcal{E}^2 - V_{\text{eff}}(r)), \tag{4.8}$$

with the effective potential

$$V_{\text{eff}}(r) = -g_{tt}\left(1 + \frac{\mathcal{L}^2}{g_{\phi\phi}}\right) = h(r)\left(1 + \frac{\mathcal{L}^2}{r^2}\right).$$

The effective potential $V_{\text{eff}}(r)$ in general relativity plays a role similar to the classical mechanics, but it incorporates the effects of spacetime curvature as well. It determines the radial motion of a test particle (massive or massless) moving in a curved spacetime. The behavior of the effective potential is depicted in Fig. 4.1. The peak corresponds to unstable circular orbits and the radius at which V_{eff} is zero corre-

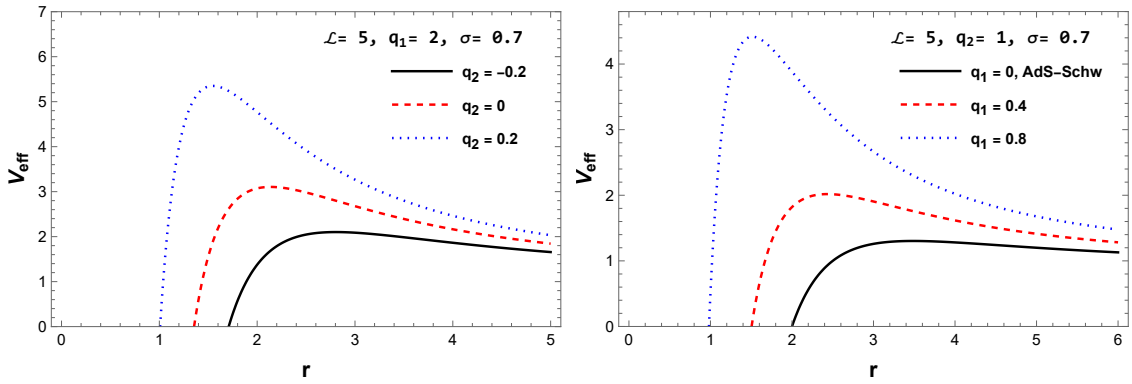

Figure 4.1 Variation of the effective potential V_{eff} with the radial coordinate r for the indicated parameter values. In the upper (lower) panel, q_1 (q_2) is fixed.

sponds to the horizon. According to the two panels, the horizon radius decreases while q_1 or q_2 increases. The case of $q_1 = 0$ corresponds to the AdS-Schwarzschild case. If, on the other hand, the particle is at a circular orbit at $r = r_0$ with θ varying, then the equation of motion (4.5) takes the form

$$g_{\theta\theta}\dot{\theta}^2 = \Theta(\theta) = -\Pi(r_0, \theta) \tag{4.9}$$

such that the conditions for a particle to have a circular orbit at $r = r_0$ and $\theta = \theta_0$ read as

$$R(r_0) = 0, \quad \left.\frac{dR(r)}{dr}\right|_{r_0} = 0 \tag{4.10}$$

which can be shown to be equivalent to the radial and polar conditions

$$\mathcal{E}^2 = V_{\text{eff}}(r_0), \quad \left.\frac{dR(r)}{dr}\right|_{r_0} = 0\,, \tag{4.11}$$

and

$$\Theta(\theta_0) = 0, \quad \left.\frac{d\Theta(\theta)}{d\theta}\right|_{\theta_0} = 0\,. \tag{4.12}$$

This polar condition on $\Theta(\theta)$ leads to zero angular momentum $\mathcal{L} = 0$, which means that there are no off-equatorial circular orbits. In the radial equations (4.10) and (4.11), one can determine the energy $\mathcal{E}$ and the angular momentum of circular orbits. Angular momentum (energy) is plotted in Fig. 4.2 in the upper (lower) two panels for different values of q_1 and q_2. When q_1 or q_2 increases, the angular momentum decreases while keeping one of them held fixed in each panel. The opposite is true for the energy. Nevertheless, in all cases, the energy and angular momentum minima are shifted towards the smaller radii as q_1 or q_2 increases. In Fig. 4.3

depicted are the allowed values of the energy and angular momentum of the particle in the circular orbits. For a fixed value of the angular momentum, the particle's energy ranges between a minimum and maximum. When they coincide, the angular momentum reaches its critic values, circled in Fig. 4.3. As q_1 increases, the critical value of angular momentum gets smaller. However, when both q_1 and q_2 are fixed, the critical angular momentum takes larger values as the Breitenlohner-Freedman parameter σ increases.

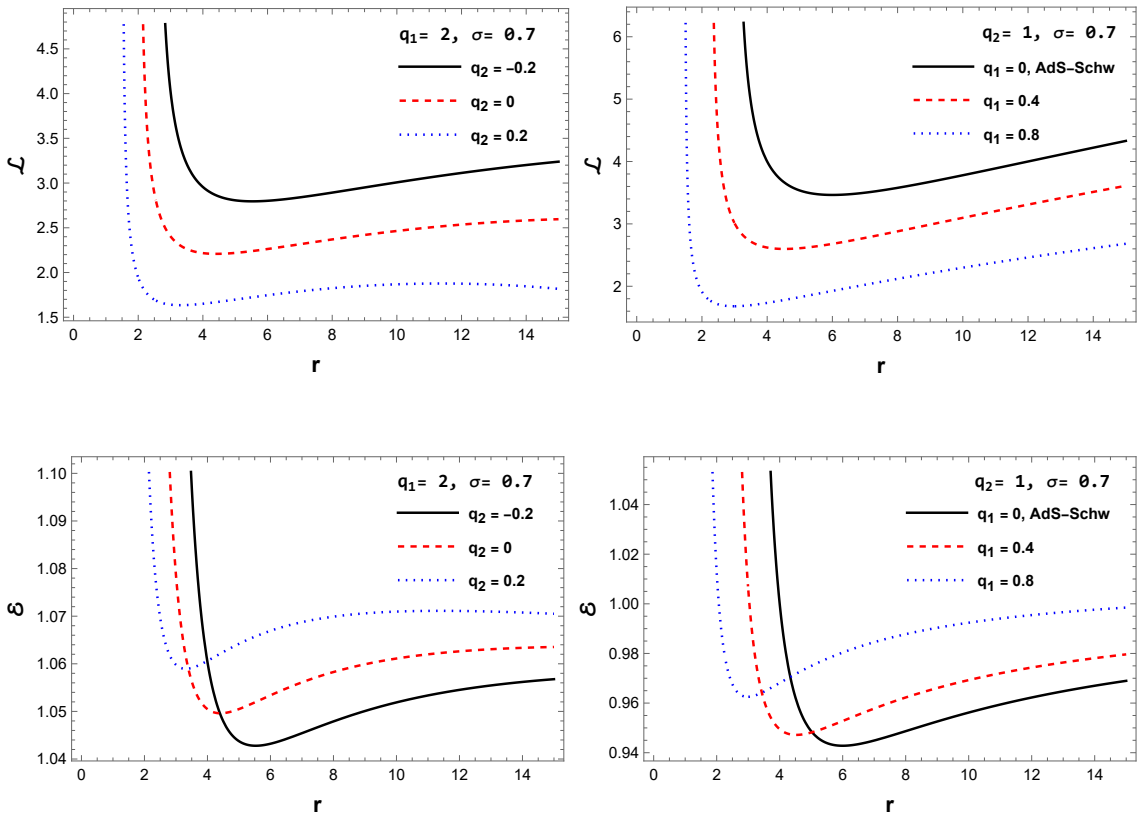

Figure 4.2 Variations of the angular momentum $\mathcal{L}$ and energy $\mathcal{E}$ with the radial coordinate r for circular orbits for the indicated values of the parameters. In the left (right) panels, q_1 (q_2) is held fixed while q_2 (q_1) takes on three different values.

In addition to the radial conditions in 4.11, the following condition should be satisfied

$$\left.\frac{d^2V_{\text{eff}}(r)}{dr^2}\right|_{r_0} = 0 \tag{4.13}$$

for determining the ISCO radius. We solve this equation using the energy and angular momentum values we found from (4.11). The resulting ISCO radii are shown in Fig. 4.4. As the figure suggests, the ISCO radius decreases as q_1 or q_2

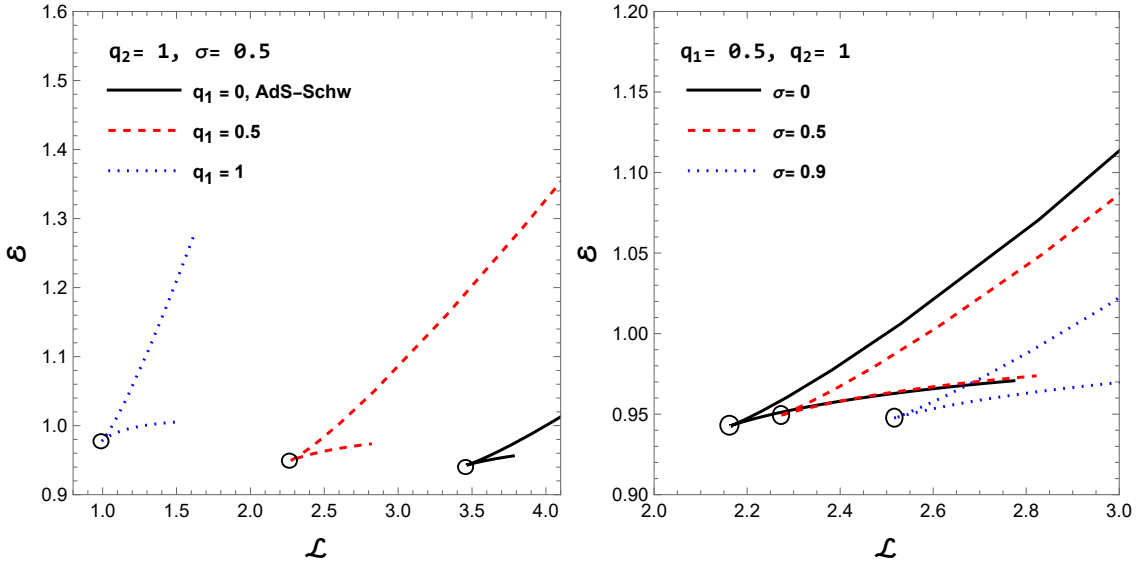

Figure 4.3 The energy $\mathcal{E}$ of the test particle around the EMPG compact object in circular orbits for specific ranges of the angular momentum $\mathcal{L}$. In the left (right) panel, q_2 and σ are held fixed while q_1 varies. In the right panel, q_1 and q_2 are fixed with σ taking on different values.

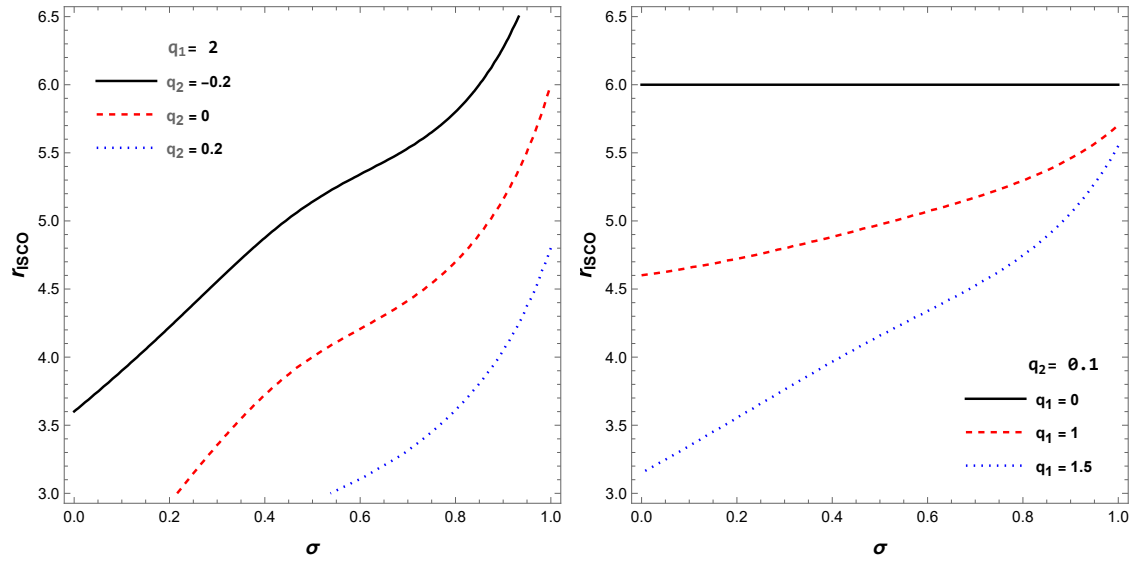

Figure 4.4 Dependence of the ISCO radius on the mass parameter σ for the indicated values of charges. In the left (right) panel, q_1 (q_2) is fixed and q_2 (q_1) takes on three different values.

increases, while the other remains fixed. However, as σ increases, the ISCO radius increases. For $q_1 = 0$, the ISCO radius remains constant and is almost equal to the Schwarzschild ISCO radius, as expected.

Fig. 4.5 illustrates how the energy and angular momentum of the test particles vary with the ISCO radius. For $q_1 = 0$, the angular momentum takes its maximum value while energy takes its minimum value, corresponding to the Schwarzschild black hole with $r_{ISCO} = 6$. As q_1 increases, the ISCO radius also increases; therefore,

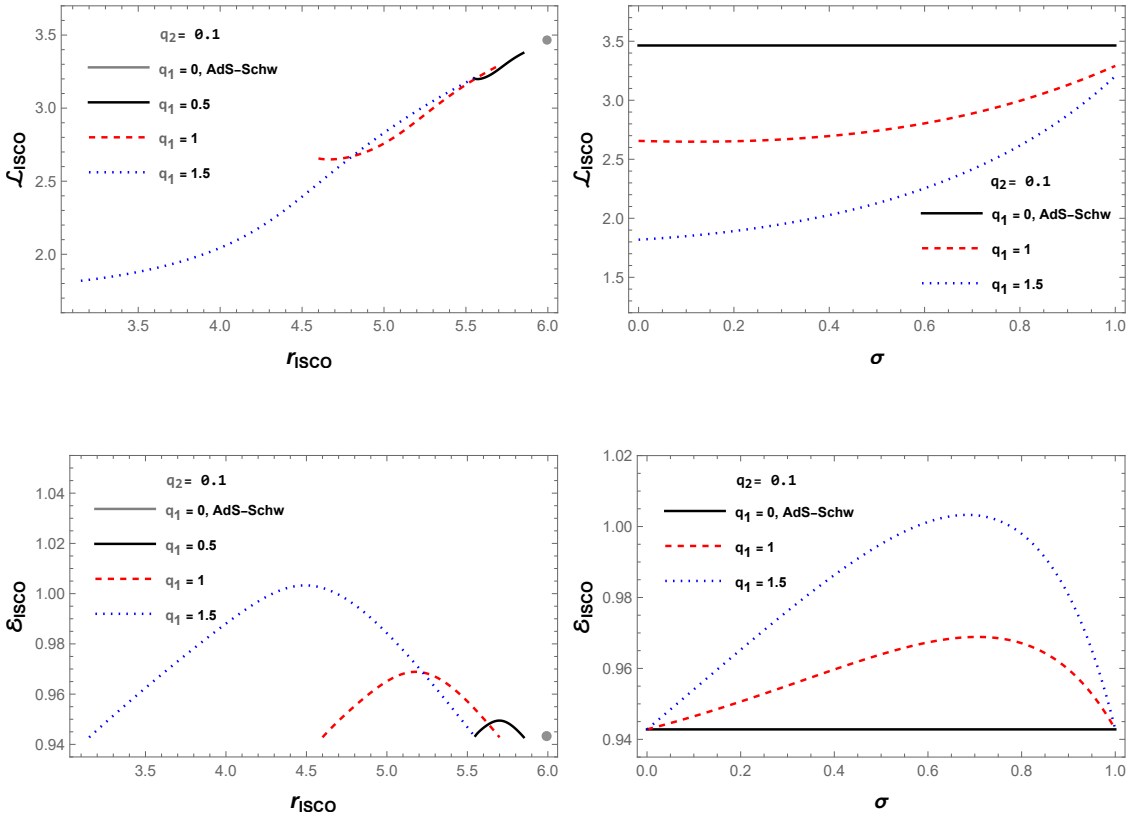

Figure 4.5 The dependencies of the energy and angular momentum of a particle (situated on ISCO) on the ISCO radius (left panels) and on the σ (right panels) for the indicated values of the Proca field parameters.

the accessible energy ranges and angular momentum get larger. For non-zero q_1, angular momentum increases with σ and gets close to the Schwarzschild case as σ tends to unity. The particle attains its minimum energy for $q_1 \neq 0$, corresponding to the Schwarzschild case at $\sigma = 0$ and $\sigma = 1$ values. The energy peak is shifted to higher values of σ as q_1 increases.

4.2 Fundamental Frequencies

This section calculates the fundamental frequencies characterizing the particle orbiting around the EMPG black holes. In particular, we focus on frequencies of Keplerian orbits and the radial and vertical oscillations. In invariant time λ (namely $\dot{t} = dt/d\lambda$), the angular velocity $\Omega_k = \dot{\phi}/\dot{t}$ of the particle,

$$\Omega_k = -\frac{g_{tt}\mathcal{L}}{g_{\phi\phi}\mathcal{E}} \tag{4.14}$$

which is nothing but the **Keplerian frequency**. The Keplerian frequency is the frequency at which a test particle moves in a circular orbit around a central mass due to gravity and it determines the main peak in QPOs. Substituting energy, angular momentum, and metric functions into (4.14) leads to the following equation for Keplerian frequency:

$$\Omega_k^2 = \frac{1}{l^2} + \frac{q_1^2(\sigma-1)^2 r^{\sigma-3}}{2(\sigma-3)} + \frac{q_1 q_2\left(\sigma^2-4\right)+6}{6r^3}. \tag{4.15}$$

Now, we study small oscillation frequencies of the test particles to characterize their deviations from the stable circular orbit at $r = r_0$ and $\theta = \theta_0$. In the equatorial plane, motion equations found in Sec.(4.1) in the radial direction read as

$$g_{rr}\dot{r}^2 = R(r)\ , \quad R(r_0) = 0\ , \quad \left.\frac{dR(r)}{dr}\right|_{r_0} = 0\,. \tag{4.16}$$

Similarly, at a fixed radius, motion equations in the polar direction read as

$$g_{\theta\theta}\dot{\theta}^2 = \Theta(\theta)\ , \quad \Theta(\theta_0) = 0\ , \quad \left.\frac{d\Theta(\theta)}{d\theta}\right|_{\theta_0} = 0\ . \tag{4.17}$$

Now, around an orbit of test particles defined by equations (4.16) and (4.17), we introduce the perturbations δr and $\delta\theta$ as

$$r = r_0 + \delta r\ , \quad \theta = \theta_0 + \delta\theta$$

and study the time development of the perturbations to determine if the orbits are stable. In fact, we can expand $R(r)$ and $\Theta(\theta)$ around the stable circular orbit (r_0, θ_0) in the form

$$\begin{aligned} R(r_0+\delta r) &= R(r_0) + R'(r_0)\delta r + \frac{1}{2}R''(r_0)\delta r^2 + \ldots, \\ \Theta(\theta_0+\delta\theta) &= \Theta(\theta_0) + \Theta'(\theta_0)\delta\theta + \frac{1}{2}\Theta''(\theta_0)\delta\theta^2 + \ldots \end{aligned} \tag{4.18}$$

where $R'(r_0) = \left.\frac{dR(r)}{dr}\right|_{r_0}$, $\Theta''(\theta_0) = \left.\frac{d^2\Theta(\theta)}{d\theta^2}\right|_{\theta_0}$ etc. The stability of the orbits requires the first two terms in these explanations to vanish so that from the equations (4.16) and (4.17), one is led to the following equations

$$g_{rr}\,\delta\dot{r}^2 = \frac{1}{2}R''(r_0)\delta r^2\ , \quad g_{\theta\theta}\,\delta\dot{\theta}^2 = \frac{1}{2}\Theta''(\theta_0)\delta\theta^2\,. \tag{4.19}$$

Now, taking derivatives of these equations for the invariant time λ and relating the invariant time to coordinate time as $\frac{d}{d\lambda} = \frac{dt}{d\lambda}\frac{d}{dt} = \dot{t}\frac{d}{dt}$ we find the following harmonic

oscillation equations

$$\frac{d^2}{dt^2}\delta r+\omega_r^2\delta r=0\ ,\quad \frac{d^2}{dt^2}\delta\theta+\omega_\theta^2\delta\theta=0$$

wherein the radial and the vertical (lateral) frequencies have the explicit expressions

$$\omega_r^2=-\frac{1}{g_{rr}\dot{t}^2}R''(r_0)\ ,\quad \omega_\theta^2=-\frac{1}{g_{\theta\theta}\dot{t}^2}\Theta''(\theta_0)\ . \tag{4.20}$$

After substituting the metric functions, $R''(r_0)$ and $\Theta''(\theta_0)$, the radial and vertical frequencies, respectively, read as

$$\begin{aligned}\omega_r^2=&\Bigg(24\left(3l^4q_1^2(\sigma-1)r^{\sigma+4}+(\sigma-3)\left(3l^2r^7\right.\right.\\&\left.\left.-l^4r^4\left(q_1q_2\left(\sigma^2-4\right)-3r+6\right)\right)\right)^{-1}\\&\left(l^2\left(3q_1^2(\sigma-1)r^\sigma+2q_1q_2\left(\sigma^2-7\right)-12(r-2)\right)-12r^3\right)\\&\Big(l^2\Big(3q_1^4(\sigma-1)^3r^{2\sigma}+q_1^2(\sigma-1)r^\sigma\left(q_1q_2(\sigma-2)(\sigma+2)\right.\\&\left.(\sigma(\sigma+4)-6)+3\left(-\left((r-2)\sigma^2\right)+r+8\sigma-12\right)\right)\\&+(\sigma-3)\left(q_1q_2\left(\sigma^2-4\right)+6\right)\left(q_1q_2\left(\sigma^2-4\right)-r+6\right)\Big)\\&-3r^3(\sigma-3)\left(q_1^2(\sigma-5)(\sigma-1)r^\sigma-5q_1q_2\left(\sigma^2-4\right)\right.\\&\left.+8r-30\right)\Big)\ ,\end{aligned} \tag{4.21}$$

$$\begin{aligned}\omega_\theta^2=&\frac{1}{6l^2r^3(\sigma-3)}\left(3l^2q_1^2(\sigma-1)^2r^\sigma\right.\\&\left.+(\sigma-3)\left(l^2\left(q_1q_2\left(\sigma^2-4\right)+6\right)+6r^3\right)\right)\ .\end{aligned} \tag{4.22}$$

In our analysis, we express all the frequencies in Hz namely, we define the epicyclic frequencies

$$\nu_i=\frac{1}{2\pi}\frac{c^3}{GM}\,\omega_i \tag{4.23}$$

where $i=(r,\theta,\phi)$, $c=3\cdot10^8$ m/sec is the speed of light in vacuum, $G=6.67\cdot10^{-11}$ m^3/(kg$^2\cdot$sec) is the gravitational Newtonian constant, and $M=10M_\odot$, $M_\odot$ being the solar mass.

Frequencies of particles in Keplerian orbits and their radial oscillation frequencies are plotted in Fig. 4.6 as a function of the radial coordinate r. In the figure, the left (right) panel is for the Keplerian (radial) frequency ν_ϕ (ν_r). The vertical line in the left panel stands for the photon sphere radius of the Schwarzschild black hole. One notes that the Keplerian frequency and lateral frequencies coincide in the equatorial plane. As the figure shows, for $q_1 > 0$, the frequencies fall below that of the Schwarzschild black hole. For the radial frequency in the lower panel, the peak moves to higher r values as q_1 gets larger. In both cases we recover the radial and lateral frequency of AdS-Schwarzschild solution by considering the limit case of $q_1 = 0$, which is shown with solid black lines.

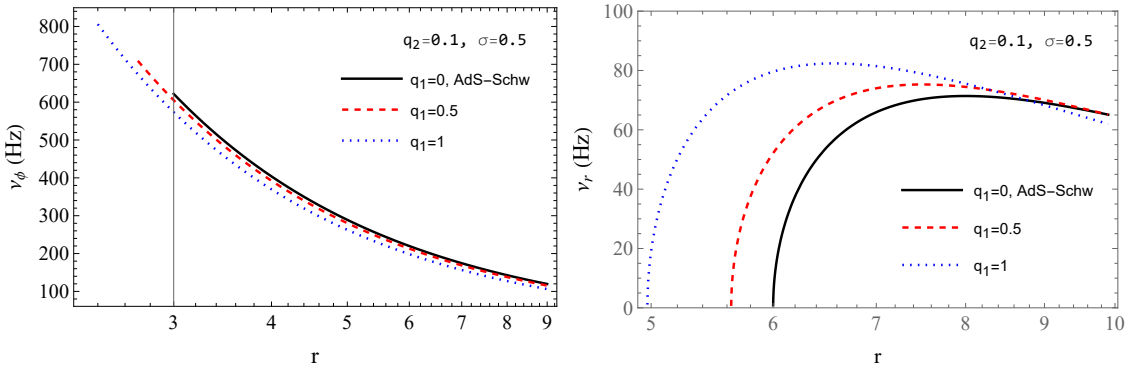

Figure 4.6 The epicyclic frequencies of the Keplerian (left panel) and radial (right panel) types for the indicated values of the EMPG parameters.

4.3 QPOs and Its Astrophysical Applications

The observed QPO frequencies (from X-ray data) are typically interpreted as combinations of the orbital frequencies of test particles around black holes. In our analysis, we have calculated the fundamental frequencies ν_ϕ, ν_r, and ν_θ for the EMPG black holes, which allows us to predict the QPO frequencies that would arise in such a spacetime.

In X-ray observations of accreting black holes, the power spectrum often exhibits two prominent peaks, referred to as *twin high-frequency QPOs*. These are labeled as the **upper frequency** ν_U and the **lower frequency** ν_L. In this section, we adopt the *Relativistic Precession Model (RP)* to relate these observed QPO frequencies to the calculated orbital frequencies of test particles.

In observational astrophysics, high-frequency quasi-periodic oscillations (HF QPOs)

hold significant importance, serving as a robust framework for predicting the parameters of black holes in accretion systems. These systems include microquasars, binaries with a stellar-mass black hole, and active galactic nuclei housing supermassive black holes. The HF QPO frequencies in microquasars typically fall within the hundreds of Hz range, while those around supermassive black holes are significantly lower, differing by orders of magnitude. The observed inverse-mass scaling in these frequencies, governed by the relationships of epicyclic frequencies in orbital motion (Remillard & McClintock, 2006), makes geodesic models of HF QPOs promising. Particularly noteworthy is their tendency to reveal themselves in rational ratios, often in a 3:2 ratio (Török, Kotrlová, Šrámková & Stuchlík, 2011), suggesting resonant phenomena. In geodesic models (Kluzniak & Abramowicz, 2001), including the electromagnetic interactions (Kološ, Tursunov & Stuchlík, 2017), both of the observed upper frequencies $\nu_{\rm u}$ and lower frequencies $\nu_{\rm l}$ are theorized to result from a combination of the orbital and epicyclic frequencies, also relevant to slender tori oscillations (Rezzolla, Yoshida & Zanotti, 2003). The geodesic models were introduced initially in the relativistic precession (RP) model, with the identification $\nu_{\rm u} = \nu_\phi = \nu_{\rm K}$ and $\nu_{\rm l} = \nu_{\rm K} - \nu_{\rm r}$ (Stella, Vietri & Morsink, 1999b). In this section, we employ epicyclic frequencies in the RP model for twin HF QPOs.

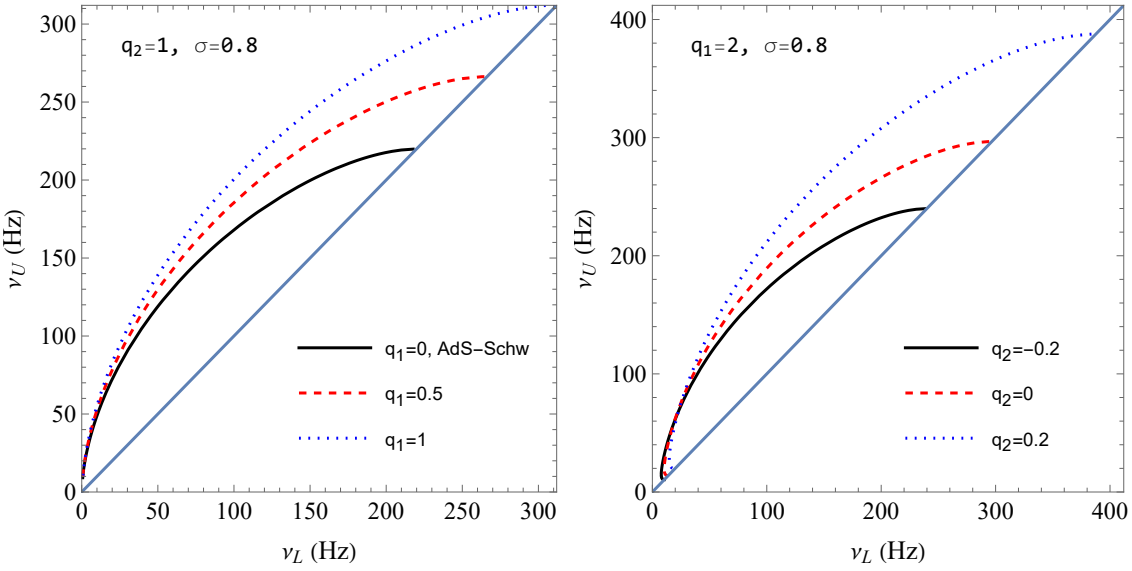

Figure 4.7 Relation between the upper and lower QPO frequencies for the indicated values of parameters q_1 and q_2. In the left (right) panel, q_2 (q_1) is held fixed, and q_1 (q_2) is allowed to take different values.

We plot the relation between the left (ν_U) and right (ν_L) frequencies of twin QPO in Fig. 4.7 for different values of q_1 and q_2. Here, we set $\sigma = 0.8$. It is observed that the frequency ratio $\nu_U : \nu_L$ grows with the increase of q_1 and q_2. The same ratio decreases for negative values of q_2. Having computed the twin QPO frequencies (ν_U and ν_L) for EMPG black holes, we are now ready to compare our results with

observational data in order to constrain the parameters of the EMPG model.

It is important to emphasize that the RP model, although widely used, is only one of several interpretations of QPOs. The physical origin of QPOs remains uncertain, and alternative scenarios exist, including disk oscillation models and other mechanisms that are not strictly dependent on relativity (Belloni & Stella, 2014; Kato, 2004; Wagoner, 1999). In this work, we adopt the RP model as a convenient framework to test modifications of relativity within EMPG gravity, and our results should be understood within this specific context rather than as a universal explanation of QPOs.

4.4 Constraining EMPG Parameters from the Twin-Peak QPO Data

In this section, we determine bounds on model parameters using the twin-peak QPO data from three different types of black hole sources: *(i)* stellar mass BH (sMBH), *(ii)* super-massive BH (SMBH), *(iii)* and intermediate-mass BH (IMBH). These black holes are, respectively, the GRO 1655-40, Sgr-A*, and M82-X1. Their observational data are documented in Table 4.1. We use these results to investigate the three black hole systems mentioned above to constrain the parameters of the EMPG model (*i.e.,* the Einstein-Geometric Proca-AdS space-time).

Table 4.1 Epicylic frequencies of the twin-peak QPOs in microquasars and galactic center.

Source [a]	ν_{U} [Hz]	$\Delta\nu_{\mathrm{U}}$ [Hz]	ν_{L} [Hz]	$\Delta\nu_{\mathrm{L}}$ [Hz]	Mass [b] [$\mathrm{M}_{\odot}$]
GRO J1655–40 (sMBH)	441	± 2	298	± 4	5.4±0.3
Sgr A* (SMBH)	(1.445	$\pm 0.16) \times 10^{-3}$	(0.886	$\pm 0.04) \times 10^{-3}$	$(4.1 \pm 0.6) \times 10^{6}$
M82-X1 (IMBH)	3.32	± 0.06	5.07	± 0.06	415 ± 63

[a] Twin-peak QPOs were first reported in Refs.Ghez, Salim, Weinberg, Lu, Do, Dunn, Matthews, Morris, Yelda, Becklin, Kremenek, Milosavljevic & Naiman (2008); Strohmayer (2001); Stuchlík & Kološ (2015).

[b] Given in Refs. Ghez et al. (2008); Strohmayer (2001); Stuchlík & Kološ (2015).

4.4.1 Monte Carlo Markov Chain (MCMC) Priors for EMPG Parameters

In this subsection, we utilize the well-equipped library `emcee` (Foreman-Mackey, Hogg, Lang & Goodman, 2013) to perform an MCMC analysis to obtain constraints on the EMPG parameters for a test particle around the compact object. In our implementation, we use the relativistic precision (RP) method.

The posterior distribution can be defined according to the standard definition (Abdulkhamidov, Nedkova, Rayimbaev & Kunz, 2024; Foreman-Mackey et al., 2013; Mitra, Vrba, Rayimbaev, Stuchlik & Ahmedov, 2024),

$$\mathcal{P}(\theta|\mathcal{D},\mathcal{M}) = \frac{P(\mathcal{D}|\theta,\mathcal{M})\pi(\theta|\mathcal{M})}{P(\mathcal{D}|\mathcal{M})} \tag{4.24}$$

where the Gaussian prior for θ is selected within appropriate limits (as listed in Table 4.2), with $\pi(\theta)$ serving as the prior distribution

$$\pi(\theta_i) \sim \exp\left[\frac{1}{2}\left(\frac{\theta_i - \theta_{0,i}}{\tilde{\sigma}_i}\right)^2\right] \tag{4.25}$$

where $\theta_{\mathrm{low},i} < \theta_i < \theta_{\mathrm{high},i}$. In our MCMC simulation of the EMPG model, the free parameters are $\theta_i = \{M, q_1, q_2, \sigma, r/M\}$ with their respective standard deviations $\tilde{\sigma}_i$. It is worth mentioning that we keep the black hole mass explicit for this analysis.

Finally, the likelihood function $\mathcal{L} = P(D|\theta,\mathcal{M})$ has the form

$$\log\mathcal{L} = \log\mathcal{L}_{\mathrm{U}} + \log\mathcal{L}_{\mathrm{L}}, \tag{4.26}$$

in which $\log\mathcal{L}_{\mathrm{U}}$ is the log-likelihood of the orbital frequency,

$$\log\mathcal{L}_{\mathrm{U}} \quad = \quad -\frac{1}{2}\sum_i \frac{(\nu^i_{\phi,\mathrm{obs}} - \nu^i_{\phi,\mathrm{th}})^2}{(\tilde{\sigma}^i_{\phi,\mathrm{obs}})^2}, \tag{4.27}$$

and $\log\mathcal{L}_{\mathrm{L}}$ stands for the log-likelihood of the periastron precession frequency (ν_{per}) as follows:

$$\log\mathcal{L}_{\mathrm{L}} = -\frac{1}{2}\sum_i \frac{(\nu^i_{\mathrm{per,obs}} - \nu^i_{\mathrm{per,th}})^2}{(\tilde{\sigma}^i_{\mathrm{per,obs}})^2}. \tag{4.28}$$

In the above, $\nu^i_{\phi,\mathrm{obs}}$ and $\nu^i_{\mathrm{per,obs}}$ are the observed values for the orbital and periastron precession frequencies ($\nu_{\mathrm{K}} = \nu_{\mathrm{U}}$) for the sources under concern. On the other hand, $\nu^i_{\phi,\mathrm{th}}$ and $\nu^i_{\mathrm{per,th}}$ stand for the values predicted by the EMPG model (see Sec. 4.2). The periastron precession frequency ν_{per} can be calculated by subtracting the radial

frequency $\nu_{\rm r}$ from the Keplerian frequency $\nu_{\rm K}$.

Table 4.2 The Gaussian priors (μ is the mean value and $\bar{\sigma}$ the variance) of the EMPG model from QPOs of the sources sMBH, SMBH, and IMBH.

Parameters	GRO J1655-40		Sgr-A*		M82-X1	
	μ	$\tilde{\sigma}$	μ	$\tilde{\sigma}$	μ	$\tilde{\sigma}$
$M\ (M_{\odot})$	5.35	0.12	4.261×10^{6}	0.072×10^{6}	417.5	5.27
$\lvert q_1\rvert$	1.25	0.15	1.37	0.10	1.25	0.11
q_2	0.18	0.07	0.13	0.09	0.25	0.08
σ	0.71	0.09	0.61	0.09	0.61	0.11
r/M	5.76	0.15	5.60	0.16	5.46	0.16

To establish the priors, we begin by examining the minimization of the Chi-square for Eq. (4.25) while setting $l = 10^{12}$, $q_1 > 1$, and $\sigma > 0.5$, where the Proca parameters have a significant effect. We explore the parameter spaces outlined in (Ghorani, Puliçe, Atamurotov, Rayimbaev, Abdujabbarov & Demir, 2023) to do this. This allows us to determine the values of the remaining parameters, M, q_2, and r/M, that result in the minimum likelihood function and ensure that the mass of the compact source closely matches the observation. This process leads us to identify the appropriate priors.

Having set the priors, we use the available data to perform an MCMC simulation to determine the plausible range of the EMPG parameters $\{M,\ q_1, q_2, \sigma,\ r/M\}$ for Einstein-Geometric Proca AdS compact object. Considering the Gaussian prior distribution, we sample 10^5 points for every parameter. This approach allows us to investigate the physically allowed multi-dimensional parameter space within defined limits and obtain the parameter values that best match the data.

4.4.2 Results of the MCMC Simulation

Using the setup described above, we investigated the 5-dimensional EMPG parameter space via an MCMC analysis for a test particle in the Einstein-Geometric Proca AdS spacetime. Note that in the MCMC simulation, we set the AdS radius parameter $l = 10^{12}$ unless otherwise noted. This way, we constrain the mass of compact objects (M), the ranges of q_1 and q_2, the mass parameter σ, and the epicyclic oscillation radius (r/M), respectively.

With this, in Fig. 4.8, Fig. 4.9, and Fig. 4.10, we give the results of the MCMC analysis of the EMPG model parameters by using the data from three different astrophysical sources. Using the *emcee* package, we obtain the posterior distribution with the possible choice of the prior given in Table 4.1. In doing so, we choose q_1 to be both positive and negative. With the higher values of $|q_1| > 1$, we notice that the mass-parameter converges to $\sigma > 0.6$, which suggests the influence of the EMPG parameter on the QPOs. However, both the choice of prior and the posterior distribution suggest the strength of q_2 to be smaller. Interestingly, for higher σ and q_1, the radius of epicyclic oscillation is converging towards $r/M < 6$, consistent with the Fig. 4.4. In all the MCMC analyses, the contour plots highlight the confidence levels ($1\tilde{\sigma}$ (68%), $2\tilde{\sigma}$ (95%) and $3\tilde{\sigma}$ (99%) of the posterior probability distributions for the entire set of parameters. The shaded regions on the contour plots reflect these confidence levels.

Table 4.3 The best-fit posterior distributions of the EMPG parameters from the QPO data.

Parameters	GRO J1655-40	Sgr-A*	M82-X1	Remark
$M\ (M_\odot)$	$5.32^{+0.11}_{-0.11}$	$4.26^{+0.07}_{-0.07} \times 10^6$	$420.10^{+5.17}_{-5.22}$	
q_1	$1.20^{+0.14}_{-0.14}$	$1.36^{+0.09}_{-0.08}$	$1.17^{+0.11}_{-0.11}$	$q_1 > 0$
q_2	$0.10^{+0.06}_{-0.06}$	$0.09^{+0.09}_{-0.09}$	$0.13^{+0.08}_{-0.07}$	
σ	$0.74^{+0.08}_{-0.09}$	$0.62^{+0.10}_{-0.09}$	$0.64^{+0.13}_{-0.10}$	
r/M	$5.68^{+0.12}_{-0.12}$	$5.57^{+0.16}_{-0.16}$	$5.54^{+0.14}_{-0.14}$	
$M\ (M_\odot)$	$5.31^{+0.11}_{-0.11}$	$4.26^{+0.07}_{-0.07} \times 10^6$	$416.84^{+5.20}_{-5.19}$	
q_1	$-1.17^{+0.14}_{-0.14}$	$-1.36^{+0.09}_{-0.09}$	$-1.19^{+0.11}_{-0.11}$	$q_1 < 0$
q_2	$-0.13^{+0.06}_{-0.06}$	$-0.09^{+0.09}_{-0.09}$	$-0.07^{+0.07}_{-0.07}$	
σ	$0.75^{+0.08}_{-0.09}$	$0.63^{+0.10}_{-0.10}$	$0.61^{+0.11}_{-0.10}$	
r/M	$5.66^{+0.12}_{-0.12}$	$5.57^{+0.16}_{-0.16}$	$5.57^{+0.13}_{-0.13}$	

More information on the best-fit values of these three parameters is given in Tab. 4.3.

However, it is worth noting that when $q_1 = 0$, the space-time simplifies to the well-known Schwarzschild AdS (Sch-AdS) space-time, which is only parametrized by l. In our MCMC implementation we did not need to explicitly treat this case separately; the code naturally recovers Sch-AdS whenever the chain samples values of q_1 sufficiently close to zero.

The MCMC analysis shows that the parameter q_1 consistently prefers non-zero values, both in the positive ($q_1 > 0$) and negative ($q_1 < 0$) regimes. Since $q_1 = 0$ cor-

responds to the Sch-AdS limit without Proca effects, these non-zero best-fit values indicate that the QPO observations are sensitive to the additional geometrical structure introduced by the Proca field. In other words, the data allows deviations from pure Sch-AdS, demonstrating that strong-gravity observations can probe the presence of vector degrees of freedom in the EMPG framework.

Here, q_1 controls the strength of the Proca field, while the mass parameter σ is constrained to moderate values ($\sigma \gtrsim 0.6$), indicating that the Proca field is dynamically relevant but neither negligible nor extremely light. These results suggest that modifications of gravity encoded in EMPG can be consistent with observational QPO data, and, while they do not provide direct evidence that EMPG replaces dark matter, they do show that such gravitational modifications are not ruled out by strong-gravity phenomena.

While the MCMC posteriors obtained for the EMPG parameters provide apparently well-defined constraints, it is important to stress that this does not automatically imply a statistical preference for EMPG over General Relativity. The extended model contains additional degrees of freedom, and with the relatively limited amount of available QPO, these parameters may simply absorb statistical fluctuations or systematics — an effect often referred to as overfitting. A rigorous model comparison using tools such as the Bayesian Information Criterion (BIC) or Bayes factors would be required to establish whether the improvement in fit is sufficient to justify the additional complexity. In the absence of such an analysis, the constraints derived here should be regarded primarily as upper limits on possible deviations from GR, rather than as evidence for non-zero EMPG parameters. A full Bayesian model selection study will therefore be a valuable extension of the present work.

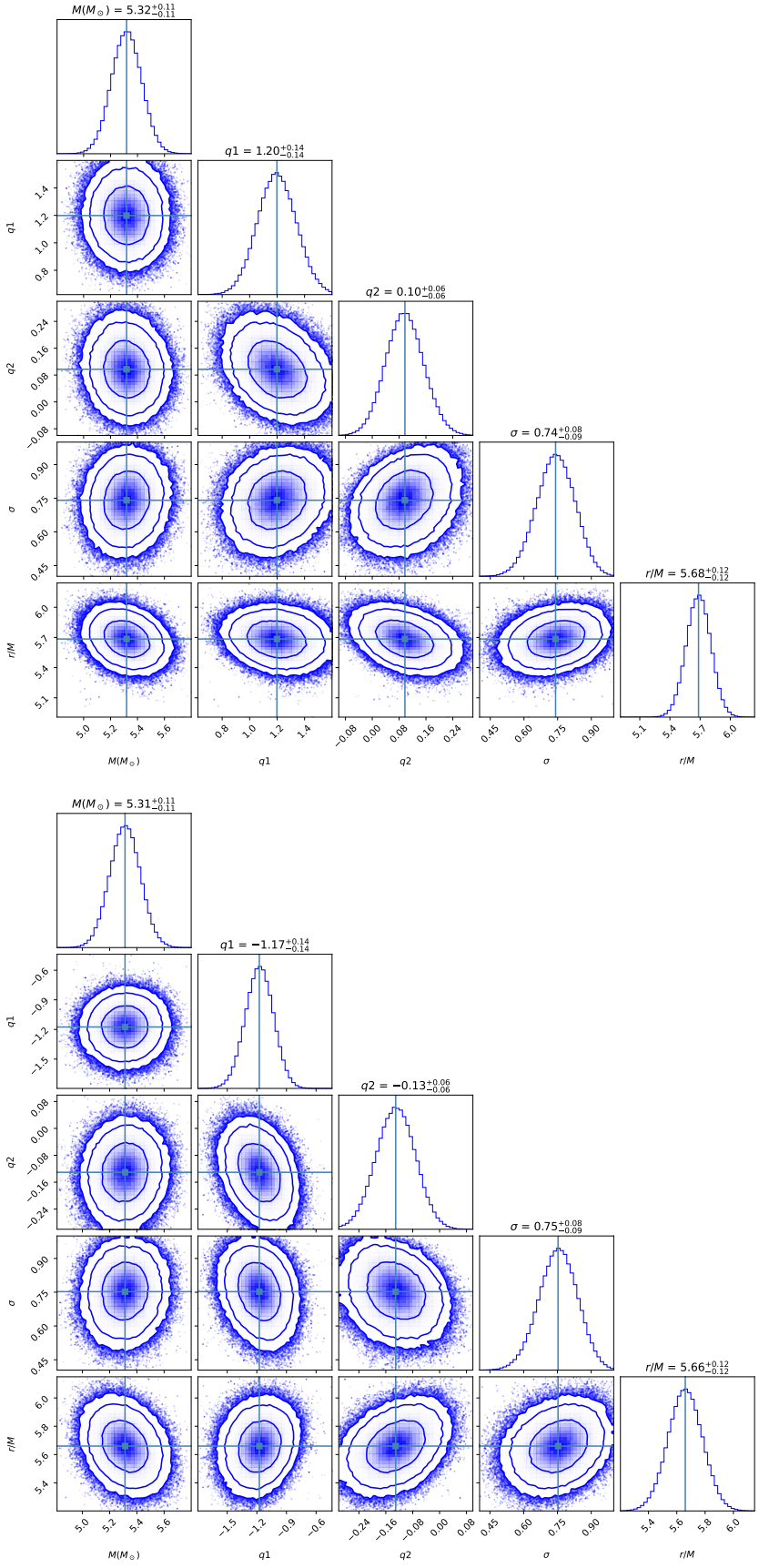

Figure 4.8 Constraints on the EMPG model parameter from a five-dimensional MCMC simulation using the state-of-the-art QPO data for the stellar-mass black hole GRO J1655-40 in the RP model. The blue contours in the upper (lower) panel correspond to $q_1 > 0$ ($q_1 < 0$).

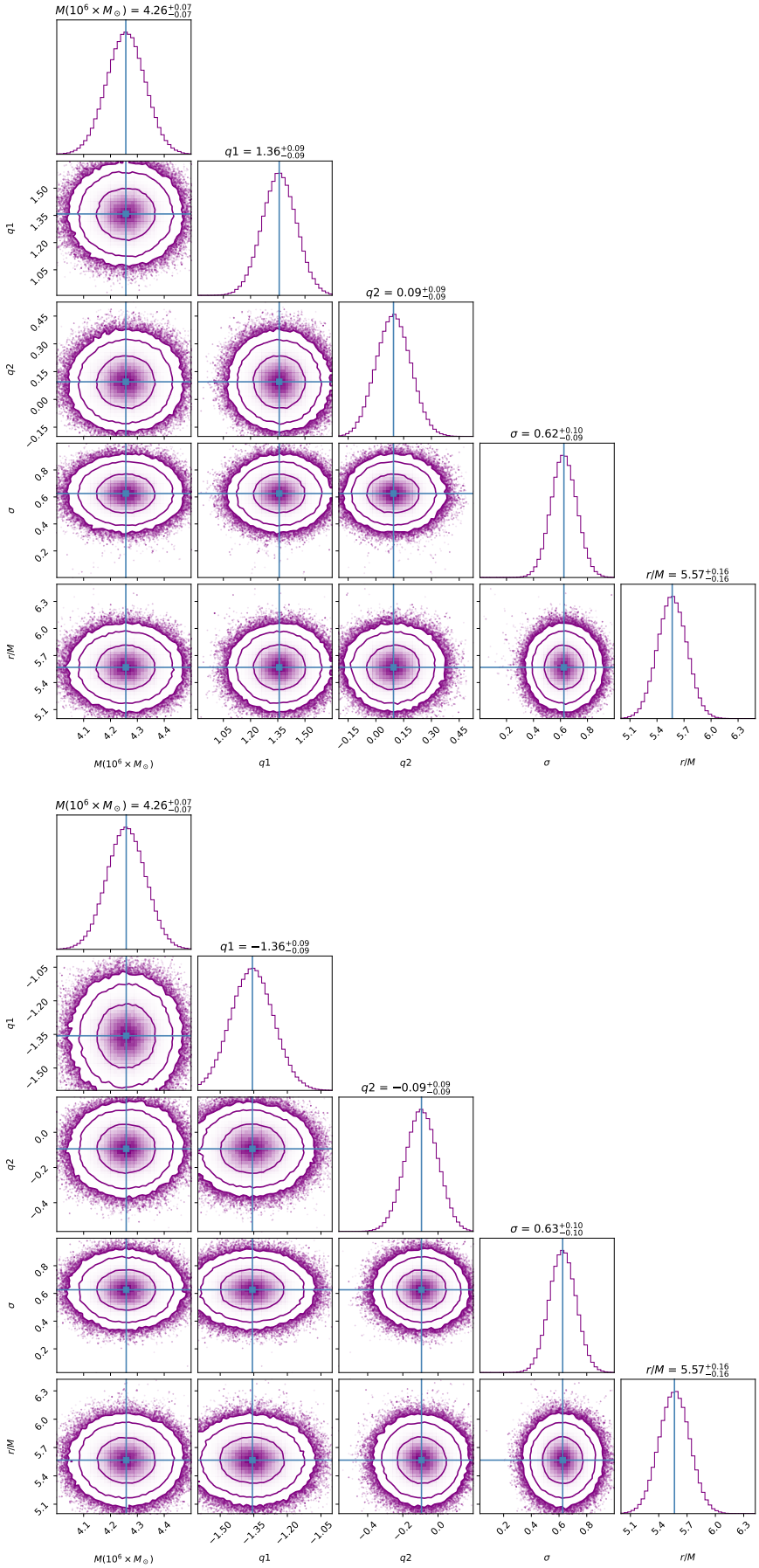

Figure 4.9 The same as in Fig. 4.8 but for the supermassive black hole Sgr-A*.

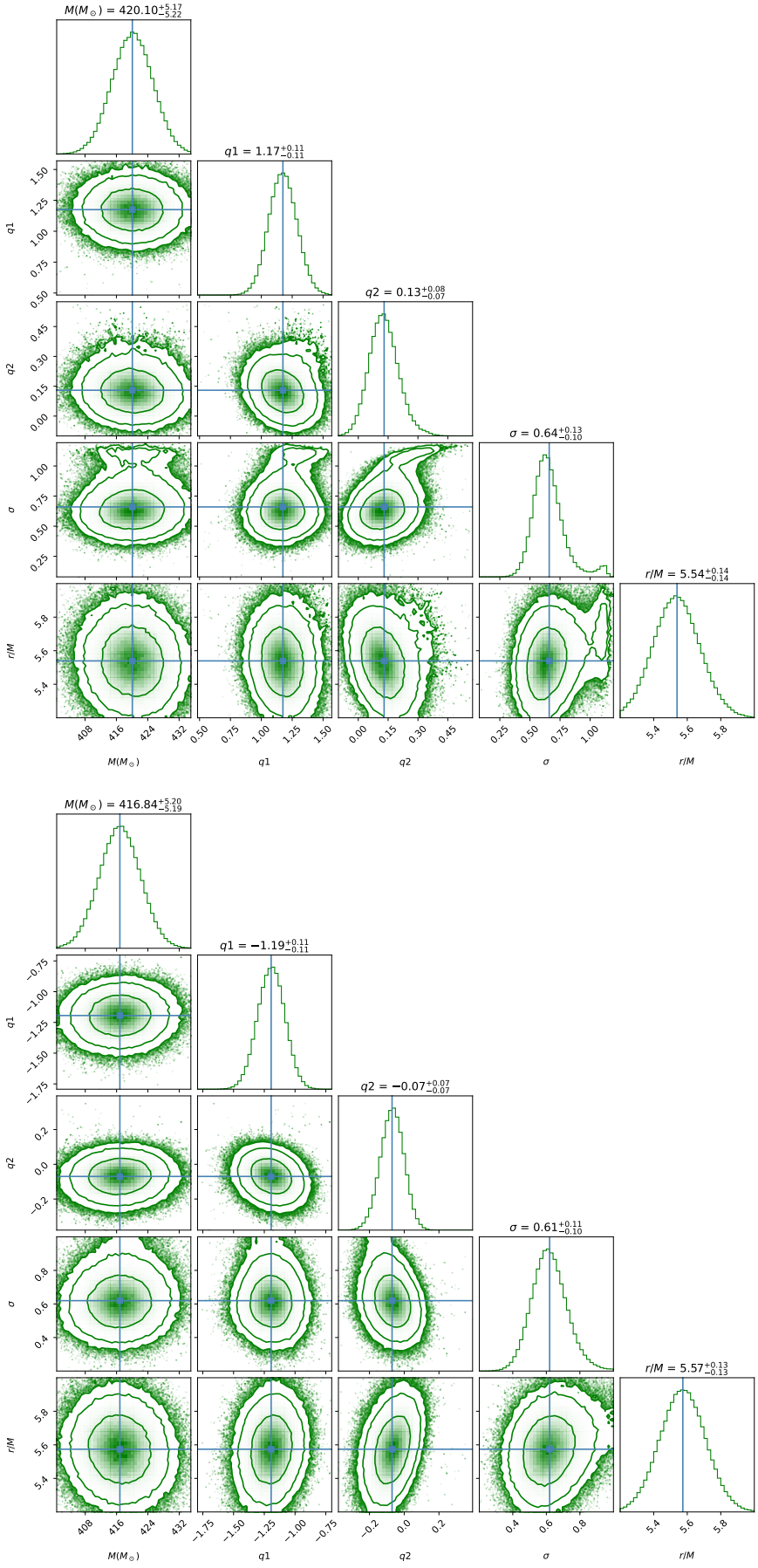

Figure 4.10 The same as in Fig. 4.8 but for the intermediate-mass black hole M82-X1.

5. SUMMARY AND CONCLUSION

In this thesis, we have performed a systematic study of the EMPG model (Demir & Puliçe, 2022) in the AdS background in the linear ghost-free limit in which quadratic and higher-order curvature terms are all dropped. The model is in the class of linear, torsion-free, metric-Palatini gravity theories (Capozziello et al., 2013b,1; Harko et al., 2012), with the extensions that a term quadratic in the antisymmetric part of the affine curvature (Demir & Puliçe, 2020; Demir & Puliçe, 2022; Vitagliano, 2014; Vitagliano et al., 2011) exists. After obtaining the black hole solution of this model, we performed a detailed investigation of shadow and photon motion around this black hole for the main purposes of probing the properties of the geometric Proca field. (As mentioned before, we use "geometric Proca" to distinguish the massive non-metricity vector of the metric-Palatini gravity from generic Einstein-Proca systems as well as the Z' gauge boson literature.) The model parameters were constrained using black hole shadow observations, followed by an analysis of particle dynamics and QPO data for further constraints.

The results obtained in this thesis can be summarized and discussed as follows:

- We have shown that the metric-Palatini gravity theory extended by antisymmetric part of the affine curvature (EMPG) reduces to the GR plus a geometrical massive vector theory—known as the Einstein–Geometric Proca (EGP) model. (Demir & Puliçe, 2020; Demir & Puliçe, 2022).

- The EMPG system provides a novel geometro-dynamical framework. It can set the stage for diversely different physical phenomena. It would certainly have effects in various astrophysical media such as neutron stars, BHs, magnetars, and other compact objects. In the present work, we study BHs with asymptotically AdS solutions which are determined by solving the EMPG field equations (2.15) and (2.16).

- Using the horizon structure of a gravitational compact object, the range of EMPG gravity parameters are also obtained in detail. It is shown that orbits enlarge or shrink depending on the value of the EMPG parameter σ. However,

the effects of parameter q_1 and q_2 are opposite to each other.

- We study the singularity structure of the EMPG black hole by analyzing the Kretschamann scalar (2.49) and the Ricci-squared scalar (2.50). Since $q_1 \to 0$ leads to the Schwarzschild solution, we simplify KS and RS expressions by expanding q_1 around zero up to the second order. The physical properties of the KS is studied and its behaviour is shown in Fig. 2.6 for various parameter values q_1 at fixed values of q_2 and σ. We show that there are basically two singularities of the KS at $r = 0$ and at the Killing horizon $r = r_H$. One can see from Fig. 2.6 that the place of the singularity at the horizon depends on the model parameters and changes accordingly. Near $q_1 = 0$, as expected, the singularities in (2.49) occur at $r = 0$ and $r = r_H = 2$, corresponding to the event horizon for the Schwarzschild black hole. It is exactly seen from the KS (2.49) that the Proca field causes the KS to deviate from the Schwarzschild limit by its charge ($q_1 \neq 0$ and $q_2 \neq 0$). The KS in the EMPG for $q_1 = q_2 \neq 0$ with σ namely $0 \leq \sigma < 1$ (ensuring $M_Y^2 \neq 0$) implies a Proca "hair" of the black hole. Given the singularity at the horizon the black hole is expected to have a “hair", and that hair is provided by the Proca field.

- We show that the EMPG model is devoid of any metric instabilities since for our model the stability related parameter is zero which makes the Lyapunov exponent imaginary. The imaginary Lyapunov exponent accordingly prevents the perturbation of the metric to diverge. The critical impact parameter b_c and the critical photon-trajectory depend on the time varying horizon radius which is dependent on the imaginary Lyapunov exponent so that for the EMPG model one expects no instability in the photon trajectory. The photon radius shows small variations about the EMPG horizon radius $r_H(0)$. Moreover, since in the EMPG model the Proca field couples minimally, one expects no instabilities arising normally from non-minimal couplings of the Proca field.

- Additionally, we have analyzed photon orbits and the influence of parameter σ. Photon sphere radius increases with σ when q_1 or q_2 is fixed. Moreover, plasma effects on photon orbits have been studied for uniform and non-uniform cases. In both cases, the photon sphere grows as the plasma frequency grows, but this effect is stronger in the uniform case.

- We have discussed the observable quantity which is the shadow of a black hole studied by the EMPG spacetime metric in vacuum and plasma. In the vacuum case, increasing the value of q_1 or q_2, when one of them held fixed, decreases the shadow size. In the presence of plasma, the shadow size decreases as the plasma frequency increases, but we have seen that, for the same values

of parameters, the photon sphere grows as plasma frequency grows. In other words, plasma brings photon sphere and shadow close to each other.

- All the results (photon orbits, BH shadow) obtained above are compared to the case of usual Schwarzschild black hole spacetime, which corresponds to case $q_1 \to 0$, parametrically. It has been shown that under the effects of the parameter q_1 the size of BH shadow gets smaller.

- We finished the shadow analysis by determining the constraints on possible values of the parameters q_1 and q_2 using the observed shadow sizes of M87* and Sgr A* for $\sigma = 0.5$ and $\sigma \to 1$. It is shown that the constraining ranges of the parameters increase with the increase of shadow size and plasma frequency.

- We continued our analysis with deriving the effective potential of a test particle orbiting Einstein-Geometric AdS black holes and determined the energy and angular momenta from it. We have shown that when $q_1 = q_2$, the angular momentum attains its critical values (see the circled dots in Fig4.3). As q_1 increases, the critical values of angular momentum and energy become smaller. However, when q_1 and q_2 are fixed, the critical angular momentum takes a larger value with the AdS mass parameter σ growth.

- We have also studied the ISCOs of the particles. We noticed when one of the charges q_1 or q_2 is kept constant, the ISCO radius decreases with an increase in q_1 or q_2. However, it gets larger as σ approaches to 1. At $q_1 = 0$, the ISCO radius remains constant for all values of q_1 & q_2 and nearly equals the ISCO radius in the Schwarzschild case, as anticipated. Moreover, in the case of $q_1 = 0$, the particle's angular momentum at the ISCO reaches its maximum value. At the same time, the energy attains its minimum value, aligning with the characteristic values in the Schwarzschild black hole having $r_{ISCO} = 6$. Also, as q_1 increases, the range for the ISCO radius expands, giving rise to a broader range of energy and angular momentum. At $q_1 \neq 0$, the ISCO angular momentum increases with $\sigma \to 1$. However, in $q_1 \neq 0$, the particle experiences its minimum energy in the ISCO, which matches the Schwarzschild case for $\sigma = 0$ and $\sigma = 1$. The peak in the energy values shifts to higher values of σ as q_1 increases.

- The expressions for the frequencies of test particles' oscillations in the radial and vertical directions along the circular stable orbits around the EMPG compact object were obtained. Our numerical analyses and graphical results have shown that the frequencies get smaller for $q_1 > 0$ than those in the Schwarzschild case. The radial and peak frequencies increase at higher

values of q_1. We studied the twin-peak QPOs in the RP model with the frequencies at hand. We have determined the relationships between the upper and lower frequencies in the twin QPOs, fixing, $\sigma = 0.8$ and observed that the frequency ratio $\nu_U : \nu_L$ gets enhanced with the increase of q_1 & q_2. In contrast, the ratio decreases for the cases $q_2 < 0$.

- Finally, we have performed a detailed MCMC analysis of the EMPG model parameters using the observational data from the twin-peak QPOs observed in the stellar-mass black hole candidate in GRO J1655-40, the intermediate-mass black hole in M82-X1, and the supermassive black hole SgA* in our Milky Way. In the MCMC analysis, we searched for the best-fit values of the EMPG parameters M, q_1, q_2, σ and r/M (radius of the QPO orbit) using the QPOs observed in the objects mentioned above. We have divided our analysis into two parts: positive values of $q_1 > 0$ and negative values of $q_1 < 0$ as presented in Figs. 4.8, 4.9, and 4.10. The shaded regions on these contour plots stand for the confidence levels.

Overall, we find that the geometric Proca, that measures the non-metricity of space-time, can be probed via the black hole observations. Our analyses show that with the increasing precision in astrophysical observations, it will be possible to pin down the model parameters like σ, q_1, and q_2 to a satisfactory level. Our solution and its phenomenological analysis can be regarded as part of a general program of constraining metric-affine gravity theories using the black hole and other observations.

BIBLIOGRAPHY

Abdulkhamidov, F., Nedkova, P., Rayimbaev, J., & Kunz, Jutta & Ahmedov, B. (2024). Parameter constraints on traversable wormholes within beyond Horndeski theories through quasiperiodic oscillations. , *109*(10), 104074.

Addazi, A., Capozziello, S., & Odintsov, S. (2021). Chaotic solutions and black hole shadow in $f(R)$ gravity. *Phys. Lett. B*, *816*, 136257.

Adler, S. L. & Pearson, R. B. (1978). "No-hair" theorems for the Abelian Higgs and Goldstone models. *Phys. Rev. D*, *18*(8), 2798–2803.

Akiyama, K. et al. (2019a). First m87 event horizon telescope results. i. the shadow of the supermassive black hole. *Astrophysical Journal Letters*, *875*, L1.

Akiyama, K. et al. (2019b). First m87 event horizon telescope results. vi. the shadow and mass of the central black hole. *Astrophysical Journal Letters*, *875*(1), L6.

Akiyama, K. et al. (2022). First Sagittarius A* Event Horizon Telescope Results. I. The Shadow of the Supermassive Black Hole in the Center of the Milky Way. *Astrophys. J. Lett.*, *930*(2), L12.

Atamurotov, F., Jusufi, K., Jamil, M., Abdujabbarov, A., & Azreg-Aïnou, M. (2021). Axion-plasmon or magnetized plasma effect on an observable shadow and gravitational lensing of a Schwarzschild black hole. *Phys. Rev. D*, *104*(6), 064053.

Ayón-Beato, E., García, A., Macías, A., & Quevedo, H. (2000). Uniqueness theorems for static black holes in metric-affine gravity. *Phys. Rev. D*, *61*(8), 084017.

Badía, J. & Eiroa, E. F. (2021). Shadow of axisymmetric, stationary, and asymptotically flat black holes in the presence of plasma. *Phys. Rev. D*, *104*(8), 084055.

Balasubramanian, V. & Kraus, P. (1999). A Stress tensor for Anti-de Sitter gravity. *Commun. Math. Phys.*, *208*, 413–428.

Bambi, C. & Freese, K. (2009). Apparent shape of super-spinning black holes. *Phys. Rev. D*, *79*, 043002.

Bardeen, J. M. (1973). Timelike and null geodesics in the kerr metric. In *Proceedings of the Ecole d'été de Physique Théorique, Les Houches*. Cited 14 times in INSPIRE as of 20 Dec 2022.

Bauer, F. & Demir, D. A. (2008). Inflation with Non-Minimal Coupling: Metric versus Palatini Formulations. *Phys. Lett. B*, *665*, 222–226.

Bauer, F. & Demir, D. A. (2011). Higgs-Palatini Inflation and Unitarity. *Phys. Lett. B*, *698*, 425–429.

Bekenstein, J. D. (1972a). Nonexistence of Baryon Number for Black Holes. II. *Phys. Rev. D*, *5*(10), 2403–2412.

Bekenstein, J. D. (1972b). Nonexistence of Baryon Number for Static Black Holes.

Phys. Rev. D, *5*(6), 1239–1246.

Belloni, T. M. & Stella, L. (2014). Fast variability from black hole binaries. *Space Science Reviews*, *183*(1-4), 43–62.

Bisnovatyi-Kogan, G. S., Tsupko, O. Y., & Perlick, V. (2019). Shadow of black holes at local and cosmological distances. *arXiv preprint arXiv:1910.10514*. Published Oct 22, 2019.

Buchdahl, H. A. (1979). REPRESENTATION OF THE EINSTEIN-PROCA FIELD BY AN A(4)*. *J. Phys. A*, *12*, 1235–1238.

Capozziello, S., Harko, T., Koivisto, T. S., Lobo, F. S. N., & Olmo, G. J. (2012). Wormholes supported by hybrid metric-Palatini gravity. *Phys. Rev. D*, *86*(12), 127504.

Capozziello, S., Harko, T., Koivisto, T. S., Lobo, F. S. N., & Olmo, G. J. (2013a). Cosmology of hybrid metric-Palatini f(X)-gravity. *JCAP*, *2013*(4), 011.

Capozziello, S., Harko, T., Koivisto, T. S., Lobo, F. S. N., & Olmo, G. J. (2013b). Hybrid f(R) theories, local constraints, and cosmic speedup. *arXiv e-prints*, arXiv:1301.2209.

Capozziello, S., Harko, T., Koivisto, T. S., Lobo, F. S. N., & Olmo, G. J. (2013c). The virial theorem and the dark matter problem in hybrid metric-Palatini gravity. *JCAP*, *2013*(7), 024.

Capozziello, S., Harko, T., Koivisto, T. S., Lobo, F. S. N., & Olmo, G. J. (2015). Hybrid Metric-Palatini Gravity. *Universe*, *1*(2), 199–238.

Demir, D. (2019). Symmergent Gravity, Seesawic New Physics, and their Experimental Signatures. *Adv. High Energy Phys.*, *2019*, 4652048.

Demir, D. (2021). Emergent Gravity as the Eraser of Anomalous Gauge Boson Masses, and QFT-GR Concord. *Gen. Rel. Grav.*, *53*(2), 22.

Demir, D. & Puliçe, B. (2020). Geometric Dark Matter. *JCAP*, *04*, 051.

Demir, D. & Puliçe, B. (2022). Geometric Proca with matter in metric-Palatini gravity. *Eur. Phys. J. C*, *82*(11), 996.

Emparan, R., Johnson, C. V., & Myers, R. C. (1999). Surface terms as counterterms in the ads/cft correspondence. *Phys. Rev. D*, *60*, 104001.

Flanagan, E. E. (2006). Fourth order Weyl gravity. *Phys. Rev. D*, *74*, 023002.

Foreman-Mackey, D., Hogg, D. W., Lang, D., & Goodman, J. (2013). emcee: The MCMC Hammer. *pasp*, *125*(925), 306.

Frolov, V. P. (1978). Massive vector fields and black holes. *Gen. Rel. Grav.*, *9*(7), 569–573.

Garcia-Saenz, S., Held, A., & Zhang, J. (2021). Destabilization of Black Holes and Stars by Generalized Proca Fields. *Phys. Rev. Lett.*, *127*(13), 131104.

Ghez, A. M., Salim, S., Weinberg, N. N., Lu, J. R., Do, T., Dunn, J. K., Matthews, K., Morris, M. R., Yelda, S., Becklin, E. E., Kremenek, T., Milosavljevic,

M., & Naiman, J. (2008). Measuring Distance and Properties of the Milky Way's Central Supermassive Black Hole with Stellar Orbits. *Astrophys. J.*, *689*, 1044–1062.

Ghorani, E., Puliçe, B., Atamurotov, F., Rayimbaev, J., Abdujabbarov, A., & Demir, D. (2023). Probing geometric proca in metric-palatini gravity with black hole shadow and photon motion. *Eur. Phys. J. C*, *83*(4), 318.

Gibbons, G. W. & Hawking, S. W. (1977a). Action Integrals and Partition Functions in Quantum Gravity. *Phys. Rev. D*, *15*, 2752–2756.

Gibbons, G. W. & Hawking, S. W. (1977b). Action integrals and partition functions in quantum gravity. *Phys. Rev. D*, *15*, 2752–2756.

Gottlieb, D., Hojman, R., Rodríguez, L. H., & Zamorano, N. (1984). Yukawa potential in a Schwarzschild background. *Nuovo Cim. B*, *80*(1), 62–70.

Harko, T., Koivisto, T. S., Lobo, F. S. N., & Olmo, G. J. (2012). Metric-Palatini gravity unifying local constraints and late-time cosmic acceleration. *Phys. Rev. D*, *85*(8), 084016.

Hehl, F. W., McCrea, J. D., Mielke, E. W., & Ne'eman, Y. (1995). Metric-affine gauge theory of gravity: field equations, Noether identities, world spinors, and breaking of dilation invariance. *physrep*, *258*(1), 1–171.

Ingram, A. R. & Motta, S. E. (2020). A review of quasi-periodic oscillations from black hole x-ray binaries: observation and theory. *New Astronomy Reviews*, *85*, 101524.

Karahan, C. N., Dogangun, O., & Demir, D. A. (2012). Conformal Transformations in Metric-Affine Gravity and Ghosts. *Annalen Phys.*, *524*, 461–469.

Kato, S. (2004). Resonant excitation of disk oscillations by warps: A model of khz qpos. *Publications of the Astronomical Society of Japan*, *56*(5), 905–922.

Kluzniak, W. & Abramowicz, M. A. (2001). Strong-Field Gravity and Orbital Resonance in Black Holes and Neutron Stars — kHz Quasi-Periodic Oscillations (QPO). *Acta Physica Polonica B*, *32*(11), 3605.

Kološ, M., Tursunov, A., & Stuchlík, Z. (2017). Possible signature of the magnetic fields related to quasi-periodic oscillations observed in microquasars. *European Physical Journal C*, *77*(12), 860.

Leaute, B. & Linet, B. (1985). Self-interaction and massive vector field in the Schwarzschild space-time. *Gen. Rel. Grav.*, *17*(8), 783–798.

Liu, H., Lü, H., & Pope, C. N. (2014). Thermodynamics of einstein–proca ads black holes. *J. High Energy Phys.*, (6), 109.

Luminet, J. P. (1979). Image of a spherical black hole with thin accretion disk. *Astronomy and Astrophysics*, *75*, 228–235.

Macías, A. & Socorro, J. (1999). Generalized Reissner-Nordström solution in metric-affine gravity. *Class. Quant. Grav.*, *16*(7), 2323–2333.

Mitra, S., Vrba, J., Rayimbaev, J., Stuchlik, Z., & Ahmedov, B. (2024). Charged

particles and quasiperiodic oscillations in Black–bounce–Reissner–Nordström geometry in braneworlds. *Physics of the Dark Universe*, *46*, 101561.

Myers, R. C. (1999). Stress tensors and casimir energies in the ads/cft correspondence. *Phys. Rev. D*, *60*, 046002.

Obukhov, Y. N. & Vlachynsky, E. J. (1999). Einstein-Proca model: spherically symmetric solutions. *Annals Phys.*, *511*(6), 497–509.

Obukhov, Y. N., Vlachynsky, E. J., Esser, W., & Hehl, F. W. (1997). Effective Einstein theory from metric-affine gravity models via irreducible decompositions. *Phys. Rev. D*, *56*(12), 7769–7778.

O'raifeartaigh, L. & Straumann, N. (2000). Gauge theory: Historical origins and some modern developments. *Rev. Mod. Phys.*, *72*(1), 1–23.

Palatini, A. (1919). Deduzione invariantiva delle equazioni gravitazionali dal principio di hamilton. *Rendiconti del Circolo Matematico di Palermo (1884-1940)*, *43*, 203–212.

Papnoi, U. & Atamurotov, F. (2022). Rotating charged black hole in 4D Einstein–Gauss–Bonnet gravity: Photon motion and its shadow. *Phys. Dark Univ.*, *35*, 100916.

Peet, A. W. (2000). TASI lectures on black holes in string theory. In *Theoretical Advanced Study Institute in Elementary Particle Physics (TASI 99): Strings, Branes, and Gravity*, (pp. 353–433).

Perlick, V. & Tsupko, O. Y. (2022). Calculating black hole shadows: Review of analytical studies. *Phys. Rept.*, *947*, 1–39.

Perlick, V., Tsupko, O. Y., & Bisnovatyi-Kogan, G. S. (2015). Influence of a plasma on the shadow of a spherically symmetric black hole. *Phys. Rev. D*, *92*(10), 104031.

Perlick, V., Tsupko, O. Y., & Bisnovatyi-Kogan, G. S. (2018). Black hole shadow in an expanding universe with a cosmological constant. *Phys. Rev. D*, *97*(10), 104062.

Rayimbaev, J., Abdujabbarov, A., & Wen-Biao, H. (2021). Regular nonminimal magnetic black hole as a source of quasiperiodic oscillations. *Phys.Rev.D*, *103*(10), 104070.

Rayimbaev, J., Bokhari, A. H., & Ahmedov, B. (2022). Quasiperiodic oscillations from noncommutative inspired black holes. *Classical and Quantum Gravity*, *39*(7), 075021.

Remillard, R. A. & McClintock, J. E. (2006). X-Ray Properties of Black-Hole Binaries. *Annual Review of Astronomy and Astrophysics*, *44*(1), 49–92.

Rezzolla, L., Yoshida, S., & Zanotti, O. (2003). Oscillations of vertically integrated relativistic tori - I. Axisymmetric modes in a Schwarzschild space-time. *mnras*, *344*(3), 978–992.

Rogers, A. (2015). Frequency-dependent effects of gravitational lensing within plasma. *Mon. Not. Roy. Astron. Soc.*, *451*(1), 17–25.

Romero, C., Fonseca-Neto, J. B., & Pucheu, M. L. (2012). General relativity and Weyl geometry. *Classical and Quantum Gravity*, *29*(15), 155015.

Scholz, E. (2017). The unexpected resurgence of Weyl geometry in late 20-th century physics. *arXiv e-prints*, arXiv:1703.03187.

Schrödinger, E. (1985). *Space-Time Structure*.

Seahra, S. S. (2005). Naked shell singularities on the brane. *Phys. Rev. D*, *71*, 084020.

Sebastiani, L., Momeni, D., Myrzakulov, R., & Odintsov, S. D. (2013). Instabilities and (anti)-evaporation of Schwarzschild–de Sitter black holes in modified gravity. *Phys. Rev. D*, *88*(10), 104022.

Sotiriou, T. P. & Faraoni, V. (2010). f(R) theories of gravity. *Reviews of Modern Physics*, *82*(1), 451–497.

Sotiriou, T. P. & Liberati, S. (2007). Metric-affine f(R) theories of gravity. *Annals Phys.*, *322*, 935–966.

Stashko, O. & Zhdanov, V. I. (2021). Singularities in Static Spherically Symmetric Configurations of General Relativity with Strongly Nonlinear Scalar Fields. *Galaxies*, *9*(4), 72.

Stella, L. & Vietri, M. (1998). Lense-Thirring Precession and Quasi-periodic Oscillations in Low-Mass X-Ray Binaries. *The Astrophys Jour Lett*, *492*(1), L59–L62.

Stella, L., Vietri, M., & Morsink, S. M. (1999a). Correlations in the Quasi-periodic Oscillation Frequencies of Low-Mass X-Ray Binaries and the Relativistic Precession Model. *The Astrophysical Journal*, *524*(1), L63–L66.

Stella, L., Vietri, M., & Morsink, S. M. (1999b). Correlations in the Quasi-periodic Oscillation Frequencies of Low-Mass X-Ray Binaries and the Relativistic Precession Model. *apjl*, *524*(1), L63–L66.

Strohmayer, T. E. (2001). Discovery of a 450 HZ Quasi-periodic Oscillation from the Microquasar GRO J1655-40 with the Rossi X-Ray Timing Explorer. *Astrophys. J*, *552*, L49–L53.

Stuchlík, Z. & Kološ, M. (2015). Mass of intermediate black hole in the source M82 X-1 restricted by models of twin high-frequency quasi-periodic oscillations. *mnras*, *451*(3), 2575–2588.

Stuchlík, Z., Slaný, P., & Hledík, S. (2000). Equilibrium configurations of perfect fluid orbiting Schwarzschild-de Sitter black holes. *Astronomy and Astrophysics*, *363*, 425–439.

Synge, J. L. (1960). *Relativity: The General Theory*. Amsterdam: North-Holland.

Török, G., Kotrlová, A., Šrámková, E., & Stuchlík, Z. (2011). Confronting the models of 3:2 quasiperiodic oscillations with the rapid spin of the microquasar GRS 1915+105. *aap*, *531*, A59.

Toussaint, M. (2000). A Numeric Solution for Einstein's Gravitational Theory with Proca Matter and Metric-Affine Gravity. *Gen. Rel. Grav.*, *32*(9), 1689–1709.

Tresguerres, R. (1995). Exact vacuum solutions of 4-dimensional metric-affine gauge theories of gravitation. *Z. Phys. C*, *65*(2), 347–354.

Tucker, R. W. & Wang, C. (1995). Black holes with Weyl charge and non-Riemannian waves. *Class. Quant. Grav.*, *12*(10), 2587–2605.

Tucker, R. W. & Wang, C. (1996). NonRiemannian gravitational interactions. In *Mathematical Aspects of Theories of Gravitation*.

Vagnozzi, S. et al. (2023). Horizon-scale tests of gravity theories and fundamental physics from the Event Horizon Telescope image of Sagittarius A. *Class. Quant. Grav.*, *40*(16), 165007.

Vitagliano, V. (2014). The role of nonmetricity in metric-affine theories of gravity. *Class. Quant. Grav.*, *31*(4), 045006.

Vitagliano, V., Sotiriou, T. P., & Liberati, S. (2010). The dynamics of generalized Palatini Theories of Gravity. *Phys. Rev. D*, *82*, 084007.

Vitagliano, V., Sotiriou, T. P., & Liberati, S. (2011). The dynamics of metric-affine gravity. *Annals of Physics*, *326*(5), 1259–1273.

Vlachynsky, E. J., Tresguerres, R., Obukhov, Y. N., & Hehl, F. W. (1996). An axially symmetric solution of metric-affine gravity. *Class. Quant. Grav.*, *13*(12), 3253–3259.

Wagoner, R. V. (1999). Relativistic diskoseismology. *Physics Reports*, *311*(3), 259–269.

Weyl, H. (1918). Gravitation und Elektrizität. *Sitzungsberichte der Kandouml;niglich Preussischen Akademie der Wissenschaften*, 465–478.

York, Jr., J. W. (1972). Role of conformal three geometry in the dynamics of gravitation. *Phys. Rev. Lett.*, *28*, 1082–1085.